

---

# From Simple to Complex: Curriculum-Guided Physics-Informed Neural Networks via Gaussian Mixture Models

---

Jianan Yang<sup>1</sup> Yiran Wang<sup>1</sup> Shuai Li<sup>1</sup> Fujun Cao<sup>2,3</sup> Xuefei Yan<sup>4</sup> Junmin Liu<sup>1</sup>

## Abstract

Physics-informed neural networks (PINNs) offer a mesh-free framework for solving partial differential equations (PDEs), yet training often suffers from gradient pathologies, spectral bias, and poor convergence, especially for problems with strong nonlinearity, sharp gradients, or multiscale features. We propose the Curriculum-Guided Gaussian Mixture Physics-Informed Neural Network (CGMPINN), which integrates Gaussian mixture modeling with dynamic curriculum learning. Specifically, a GMM is periodically fitted to the PDE residual distribution to quantify spatially varying learning difficulty. A smooth curriculum schedule progressively shifts training focus from easy to harder regions, while precision-based variance modulation suppresses unreliable clusters during early optimization. This dual curriculum is governed by a shared curriculum parameter and can be combined with self-adaptive loss balancing. We further establish theoretical guarantees, including sublinear convergence of the gradient norm for the induced time-varying loss, uniform equivalence between the curriculum-weighted and standard PDE losses, and a generalization bound with an explicit weighting-induced bias characterization. Experiments on six benchmark PDEs spanning elliptic, parabolic, hyperbolic, advection-dominated, and nonlinear reaction-diffusion types show that CGMPINN consistently achieves the lowest relative  $L_2$  and maximum absolute errors among all compared methods, reducing relative  $L_2$  error by up to 97.8% over the standard PINN at comparable cost. Our code is publicly available at <https://github.com/Mathematics-Yang/CGMPINN>.

---

<sup>1</sup>Xi'an Jiaotong University, Xi'an, China <sup>2</sup>College of International Business, Zhejiang Yuexiu University, Shaoxing, China <sup>3</sup>Shaoxing Key Laboratory of Intelligent Monitoring and Prevention of Smart Society, Shaoxing, China <sup>4</sup>Institute of Systems Engineering, AMS, Beijing, China. Correspondence to: Junmin Liu <junminliu@mail.xjtu.edu.cn>.

## 1. Introduction

Partial differential equations (PDEs) are the foundational mathematical language for modeling complex physical phenomena across scientific and engineering disciplines [1, 2]. Classical numerical methods such as the finite difference method (FDM), finite element method (FEM), and spectral methods [3, 4] have achieved remarkable success, yet encounter inherent difficulties in high-dimensional problems, multi-scale systems, complex geometries, and inverse problems with sparse and noisy data [5, 6].

Motivated by these challenges, physics-informed neural networks (PINNs), pioneered by Raissi et al. [1], have emerged as a promising mesh-free paradigm for PDE solving. PINNs encode governing PDEs and initial/boundary conditions (I/BCs) as soft regularization terms in the loss function of a neural network [7, 8]. By minimizing a composite loss combining data misfit and PDE residual, PINNs learn continuous, mesh-free solution approximations without requiring large labeled datasets [9, 10], enabling diverse applications in fluid mechanics [11], biomedical engineering [12], geophysical inversion [13], and nano-optics [14], as reviewed in [2, 15].

However, vanilla PINNs exhibit well-documented failure modes. Imbalanced gradients between the PDE residual loss and the I/BCs loss can lead to stiff gradient flow and convergence to suboptimal minima [16, 17], particularly for PDEs with strong nonlinearity, convection dominance, or multi-scale features [18, 19]. In addition, the non-convex loss landscape, poor conditioning of the optimization problem, spectral bias of neural networks [20, 21], and static uniform sampling of collocation points [22, 23] further degrade solution accuracy.

Extensive research has been devoted to addressing these issues. Wang et al. [16] proposed gradient-statistics-based learning rate annealing for adaptive loss balancing, followed by other adaptive loss weighting [24, 25] and gradient normalization techniques [26]. Yu et al. [27] introduced gPINN, a gradient-enhanced formulation incorporating PDE derivative information into training. Tao et al. [28] developed LNN-PINN, a liquid residual gating architecture, to improve predictive accuracy. Dodge et al. [29] developed STAR-

PINN, a stacked adaptive residual architecture, to enhance convergence stability and computational efficiency. From the sampling perspective, Wu et al. [23] presented a comprehensive study of sampling strategies for physics-informed neural networks, covering both non-adaptive and residual-based adaptive schemes, while Daw et al. [22] proposed the retain-resample-release (R3) framework. Importance sampling [30, 31] and Gaussian mixture distribution-based methods [32] have also been explored for targeted collocation point placement. Additionally, domain decomposition approaches [33, 34] and causal training strategies [35] address optimization complexity and temporal causality, respectively, while Bayesian extensions [36] and adversarial learning-based methods [37] have been explored for uncertainty quantification.

Among these strategies, curriculum learning (CL) [38] has emerged as a particularly effective paradigm that progressively increases problem difficulty during training. While Krishnapriyan et al. [18] confirmed the lack of universal effectiveness of fixed-step curriculum learning across multiple benchmarks, recent studies have demonstrated that dynamic curriculum regularization, integrated with early stopping mechanisms, can significantly enhance PINN training [39, 40]. More recently, curriculum-enhanced adaptive sampling [41] and adaptive task decomposition strategies [42] have integrated progressive scheduling with residual-based refinement. However, most existing curriculum methods rely on manually predefined, fixed-step schedules requiring extensive problem-specific tuning [18, 39], and even dynamic schemes [40] primarily adjust global PDE parameters without quantifying the spatially varying difficulty. To effectively capture such localized and multi-modal error landscapes, Gaussian mixture models (GMMs) provide a principled way to identify regions with heterogeneous residual structure, uncertainty, and learning difficulty. Although GMMs have been successfully employed for adaptive sampling [22, 23, 30–32], their use as an explicit mechanism for curriculum learning in PINNs remains limited. This motivates a data-driven curriculum strategy in which probabilistic information extracted from the residual distribution is used to organize training from easier regions to more difficult ones.

Based on this insight, we propose the Curriculum-Guided Gaussian Mixture Physics-Informed Neural Network (CGMPINN), a unified framework that integrates Gaussian mixture modeling with dynamic curriculum learning for PINN training. The main contributions of this work are summarized as follows:

- We propose CGMPINN, a unified framework that integrates Gaussian mixture modeling with dynamic curriculum learning for PINN training. A GMM is periodically fitted to the PDE residual distribution to quantify

spatially varying learning difficulty, and a smooth curriculum schedule progressively shifts training focus from easy to hard regions. A precision-based variance modulation mechanism further suppresses unreliable clusters during early optimization. The entire curriculum is governed by a single shared parameter and can be seamlessly combined with self-adaptive loss balancing.

- We establish three formal theoretical guarantees for CGMPINN: (i) uniform equivalence between the curriculum-weighted and standard PDE losses; (ii) sub-linear convergence of the gradient norm for the induced time-varying total loss under summable objective drift; and (iii) a Rademacher-complexity-based generalization bound for the weighted empirical PDE loss, together with an explicit characterization of the weighting-induced bias.
- We conduct systematic experiments on six benchmark PDEs spanning elliptic (1D and 2D), parabolic, hyperbolic, advection-dominated, and nonlinear reaction-diffusion regimes. Under identical architectures and training settings, CGMPINN consistently outperforms the standard PINN [1], IbPINN [25], gPINN [27], LNN-PINN [28], and STAR-PINN [29] across all error metrics, reducing the relative  $L_2$  error by up to 97.8% at comparable computational cost. An ablation study further confirms the complementary roles of the GMM-based difficulty quantification and the curriculum scheduling components.

The remainder of this paper is organized as follows. Section 2 presents the proposed CGMPINN framework, including the curriculum-guided Gaussian mixture module, self-adaptive loss balancing, and the theoretical analysis of convergence, loss equivalence, and generalization. Section 3 details the numerical experiments and comparative results. Section 4 concludes the paper and discusses future directions.

## 2. CGMPINN Framework

In this section, we present the CGMPINN framework. Following the problem formulation and a brief review of standard PINNs, we detail the two core components of our proposed approach: a *curriculum-guided Gaussian mixture* (CGM) module for difficulty-aware residual weighting, and an optional Relative Loss Balancing with Random Lookback (ReLoBRaLo)-based self-adaptive loss balancing mechanism. The CGM module jointly exploits GMM posterior responsibilities, component-level precision, and a smooth easy-to-hard curriculum schedule. The end-to-end architecture is illustrated in Figure 1.

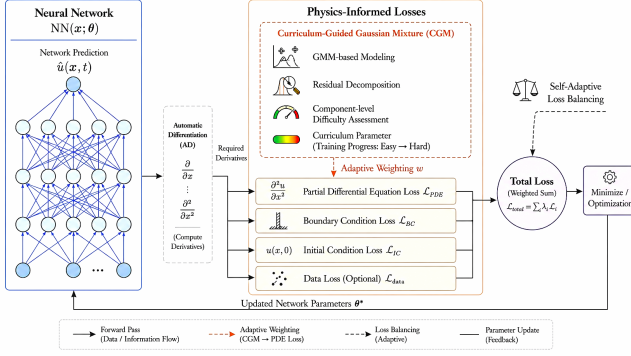


Figure 1. Architecture of the CGMPINN framework: a neural network approximator, automatic differentiation for PDE-compliant derivatives, the CGM module (GMM fitting, precision modulation, and curriculum scheduling), and an optional self-adaptive loss balancing mechanism.

## 2.1. Problem Formulation

We consider a general initial-boundary value problem on a bounded Lipschitz domain  $\Omega \subset \mathbb{R}^d$  ( $d$  is the spatial dimension) over  $[0, T]$ :

$$\begin{cases} \mathcal{D}[u](\mathbf{x}, t) = f(\mathbf{x}, t), & (\mathbf{x}, t) \in \Omega \times [0, T], \\ \mathcal{B}[u](\mathbf{x}, t) = g(\mathbf{x}, t), & (\mathbf{x}, t) \in \partial\Omega \times [0, T], \\ u(\mathbf{x}, 0) = u_0(\mathbf{x}), & \mathbf{x} \in \Omega, \end{cases} \quad (1)$$

where  $\mathbf{x} \in \Omega$  denotes the spatial coordinate,  $t \in [0, T]$  is the time variable with final time  $T > 0$ ,  $u : \Omega \times [0, T] \rightarrow \mathbb{R}$  is the unknown scalar field,  $\mathcal{D}$  is a possibly nonlinear differential operator,  $\mathcal{B}$  encodes boundary conditions (Dirichlet, Neumann, or Robin),  $\partial\Omega$  denotes the boundary of  $\Omega$ ,  $f$  is the source term,  $g$  is the boundary data, and  $u_0$  is the initial condition. For stationary problems the temporal dependence and initial condition are omitted.

## 2.2. Standard PINN Formulation and Limitations

In the PINN framework [1], the solution is approximated by  $\hat{u}(\mathbf{x}, t) = \text{NN}(\mathbf{x}, t; \theta)$ , where  $\text{NN}(\cdot; \theta)$  denotes a neural network (e.g., a fully-connected feedforward network in our experiments) with trainable parameters  $\theta \in \mathbb{R}^p$ . Automatic differentiation [43] provides the fundamental mechanism for computing exact derivatives in the residual-based optimization of physics-informed neural networks. Given  $N_\Omega$  interior collocation points  $\{(\mathbf{x}_i, t_i)\}_{i=1}^{N_\Omega}$ ,  $N_{\partial\Omega}$  boundary points  $\{(\mathbf{x}_j, t_j)\}_{j=1}^{N_{\partial\Omega}}$ , and  $N_{\text{IC}}$  initial-condition points  $\{\mathbf{x}_l\}_{l=1}^{N_{\text{IC}}}$ , the pointwise residuals are defined as

$$r_{\text{PDE}}(\mathbf{x}_i, t_i; \theta) = \mathcal{D}[\hat{u}](\mathbf{x}_i, t_i) - f(\mathbf{x}_i, t_i), \quad (2)$$

$$r_{\text{BC}}(\mathbf{x}_j, t_j; \theta) = \mathcal{B}[\hat{u}](\mathbf{x}_j, t_j) - g(\mathbf{x}_j, t_j), \quad (3)$$

$$r_{\text{IC}}(\mathbf{x}_l; \theta) = \hat{u}(\mathbf{x}_l, 0) - u_0(\mathbf{x}_l). \quad (4)$$

For notational brevity, we write  $r_{\text{PDE},i} = r_{\text{PDE}}(\mathbf{x}_i, t_i; \theta)$ , and similarly  $r_{\text{BC},j}$  and  $r_{\text{IC},l}$  for the boundary and initial-condition residuals at their respective points. The standard training objective is the composite MSE loss

$$\begin{aligned} \mathcal{L}_{\text{total}}(\theta) = & \frac{1}{N_\Omega} \sum_{i=1}^{N_\Omega} r_{\text{PDE},i}^2 + \lambda_{\text{BC}} \frac{1}{N_{\partial\Omega}} \sum_{j=1}^{N_{\partial\Omega}} r_{\text{BC},j}^2 \\ & + \lambda_{\text{IC}} \frac{1}{N_{\text{IC}}} \sum_{l=1}^{N_{\text{IC}}} r_{\text{IC},l}^2, \end{aligned} \quad (5)$$

where  $\lambda_{\text{BC}}, \lambda_{\text{IC}}$  are fixed penalty weights. Despite its elegance, this formulation has well-documented limitations: fixed weights cannot adapt to evolving gradient magnitudes, leading to gradient pathologies [16]; moreover, all collocation points are treated uniformly regardless of learning difficulty, causing the optimizer to be overwhelmed by hard residuals early in training and often converging to suboptimal local minima [18]. CGMPINN addresses both challenges through the mechanisms detailed below.

## 2.3. Curriculum-Guided Gaussian Mixture Module

The CGM module is the core of CGMPINN. It fits a Gaussian mixture model (GMM) to the PDE residuals, extracting three complementary information channels: (i) *posterior responsibilities* (latent variables) that softly assign each collocation point to mixture components; (ii) *component-level difficulty* derived from responsibility-weighted residual magnitudes; and (iii) *component-level precision* (inverse variance) that quantifies the reliability of each cluster. A smooth curriculum schedule then combines these signals to transition training progressively from easy, well-conditioned residual regions to hard, uncertain ones.

### 2.3.1. RESIDUAL DISTRIBUTION MODELING VIA GMM

At training iteration  $k$ , the PDE residuals at all  $N_\Omega$  interior collocation points, evaluated at the network parameters  $\theta_{k-1}$  obtained from the previous iteration, are collected as

$$\mathcal{R}^{(k)} = \{r_i \triangleq r_{\text{PDE}}(\mathbf{x}_i, t_i; \theta_{k-1})\}_{i=1}^{N_\Omega}. \quad (6)$$

Their distribution is modeled by a  $K$ -component Gaussian mixture

$$p(r) = \sum_{m=1}^K \pi_m \mathcal{N}(r | \mu_m, \sigma_m^2), \quad (7)$$

where  $\pi_m \geq 0$ ,  $\sum_m \pi_m = 1$  are mixing coefficients and  $(\mu_m, \sigma_m^2)$  are the mean and variance of the  $m$ -th component. The parameters  $\Theta_{\text{GMM}} = \{\pi_m, \mu_m, \sigma_m^2\}_{m=1}^K$  are estimated via the Expectation-Maximization (EM) algorithm. Upon convergence, the posterior responsibility of component  $m$  for sample  $r_i$  is

$$\gamma_{im} = \frac{\pi_m \mathcal{N}(r_i | \mu_m, \sigma_m^2)}{\sum_{l=1}^K \pi_l \mathcal{N}(r_i | \mu_l, \sigma_l^2)}. \quad (8)$$

These posterior responsibilities serve as *soft latent assignments*, indicating the degree to which each collocation point belongs to each mixture component, and form the bridge connecting component-level information to sample-level weights.

### 2.3.2. DIFFICULTY QUANTIFICATION, PRECISION MODULATION, AND CURRICULUM SCHEDULING

**Component-level difficulty.** The difficulty of the  $m$ -th Gaussian component is quantified as the posterior-weighted mean squared residual:

$$d_m = \frac{\sum_{i=1}^{N_\Omega} \gamma_{im} r_i^2}{\sum_{i=1}^{N_\Omega} \gamma_{im} + \epsilon}, \quad (9)$$

where  $\epsilon > 0$  is a small positive constant introduced throughout this section to prevent division by zero in normalization and weighting steps. Components with large  $d_m$  correspond to regions where the current network produces large PDE residuals and are thus deemed more difficult. To enable comparable scaling, the scores are normalized to the unit interval:

$$\tilde{d}_m = \frac{d_m - d_{\min}}{d_{\max} - d_{\min} + \epsilon}, \quad (10)$$

where  $d_{\min} = \min_m d_m$  and  $d_{\max} = \max_m d_m$ .

**Curriculum parameter.** A curriculum parameter  $\tau(k) \in [0, 1]$  increases monotonically with training iteration  $k$ , governing the smooth transition from easy-sample focus to hard-sample focus:

$$\tau(k) = \min\left(\frac{k}{k_{\max} \cdot c_{\text{sat}}}, 1\right), \quad (11)$$

where  $k_{\max}$  is the total number of iterations and  $c_{\text{sat}} \in (0, 1]$  is the saturation fraction that specifies the proportion of training at which  $\tau$  reaches unity. For notational convenience, we suppress the iteration index and write  $\tau$  in place of  $\tau(k)$  in subsequent expressions.

**Curriculum-controlled component weights.** For each component  $m$ , an easy-favoring weight and a hard-favoring weight are defined via exponential mappings:

$$w_m^{\text{easy}} = \exp(-\beta \tilde{d}_m), \quad w_m^{\text{hard}} = \exp(-\beta(1 - \tilde{d}_m)), \quad (12)$$

where  $\beta > 0$  controls the intensity of discrimination between easy and hard components. The CL weight for component  $m$  is the  $\tau$ -controlled convex combination:

$$w_m^{\text{CL}}(\tau) = (1 - \tau) w_m^{\text{easy}} + \tau w_m^{\text{hard}}. \quad (13)$$

**Precision-based variance modulation.** Beyond the difficulty scores derived from residual magnitudes, the GMM provides component-level variance estimates  $\sigma_m^2$  that encode the *spread* of residuals within each cluster. We exploit the inverse variance (precision) as a complementary

reliability indicator. The normalized precision factor for component  $m$  is

$$v_m = \frac{(\sigma_m^2 + \epsilon)^{-1}}{\max_{1 \leq l \leq K} (\sigma_l^2 + \epsilon)^{-1}} \in (0, 1]. \quad (14)$$

Components with small variance yield  $v_m \approx 1$ , indicating tightly concentrated, reliably learnable residual clusters; components with large variance yield small  $v_m$ , reflecting dispersed, uncertain residuals that may destabilize early-stage optimization. To maintain curriculum compatibility, the precision factor is itself modulated by the curriculum parameter  $\tau$ :

$$\tilde{v}_m(\tau) = (1 - \tau) v_m + \tau. \quad (15)$$

During early training ( $\tau \approx 0$ ), the full precision weighting suppresses high-variance components, prioritizing stable learning regions. As training progresses ( $\tau \rightarrow 1$ ), the modulation smoothly fades to unity, allowing all components—including previously suppressed uncertain regions—to contribute equally once the network has established a reliable baseline.

The final component-level (comp) weight integrates both the curriculum difficulty weight and the precision modulation:

$$w_m^{\text{comp}}(\tau) = w_m^{\text{CL}}(\tau) \cdot \tilde{v}_m(\tau). \quad (16)$$

This design achieves a *dual curriculum*: along the difficulty dimension, the network progresses from easy to hard residual regions; along the reliability dimension, it progresses from well-conditioned (low-variance) to uncertain (high-variance) clusters. Both transitions are synchronized through the shared curriculum parameter  $\tau$ .

**Sample-level weights.** The per-sample weight for the  $i$ -th collocation point is obtained by aggregating the component-level weights through the posterior responsibilities:

$$w_i = \sum_{m=1}^K \gamma_{im} w_m^{\text{comp}}(\tau), \quad (17)$$

and is subsequently normalized to unit mean to preserve the overall loss magnitude:

$$w_i \leftarrow \frac{N_\Omega \cdot w_i}{\sum_{j=1}^{N_\Omega} w_j + \epsilon}. \quad (18)$$

The curriculum-weighted PDE loss evaluated at the current parameters  $\theta$  is then

$$\mathcal{L}_{\text{PDE}}^w(\theta) = \frac{1}{N_\Omega} \sum_{i=1}^{N_\Omega} w_i r_{\text{PDE},i}^2, \quad (19)$$

where  $r_{\text{PDE},i} = r_{\text{PDE}}(\mathbf{x}_i, t_i; \theta)$  denotes the residual at the current parameters  $\theta$  (over which the gradient is taken), and

the weights  $\{w_i\}$  are computed from the snapshot residuals  $\{r_i\}$  at the previous parameters  $\theta_{k-1}$  and held fixed during the current gradient step. In practice, the GMM parameters and sample weights are re-estimated every  $k_{\text{upd}}$  iterations to adapt to the evolving residual landscape.

#### 2.4. Self-Adaptive Loss Balancing via ReLoBRaLo

To mitigate gradient imbalance among different loss components, the CGMPINN framework optionally integrates the Relative Loss Balancing with Random Lookback (ReLoBRaLo) mechanism [25]. Suppose the total loss consists of  $C$  components (e.g.,  $C = 3$  for the PDE, boundary, and initial-condition terms), and let  $L_c(k)$  denote the value of the  $c$ -th loss component ( $\mathcal{L}_{\text{PDE}}^w$ ,  $\mathcal{L}_{\text{BC}}$ ,  $\mathcal{L}_{\text{IC}}$ , respectively) at iteration  $k$ . ReLoBRaLo maintains an exponential moving average (EMA)

$$\bar{L}_c(k) = \alpha \bar{L}_c(k-1) + (1-\alpha) L_c(k), \quad (20)$$

with smoothing coefficient  $\alpha \in (0, 1)$ . At each iteration, a reference loss  $L_c^{\text{ref}}(k)$  is defined as

$$L_c^{\text{ref}}(k) = \begin{cases} \bar{L}_c(k-1), & \text{with probability } \rho, \\ L_c(k'), & \text{otherwise,} \end{cases} \quad (21)$$

where  $\rho \in (0, 1)$  and  $k' < k$  is a uniformly sampled historical iteration (random lookback). The adaptive weight is computed via a  $\kappa$ -scaled softmax over the relative ratios  $\varrho_c(k) = L_c(k)/(L_c^{\text{ref}}(k) + \epsilon)$ :

$$\lambda_c(k) = C \cdot \frac{\exp(\varrho_c(k)/\kappa)}{\sum_{c'=1}^C \exp(\varrho_{c'}(k)/\kappa)}, \quad (22)$$

where  $\kappa > 0$  is the softmax temperature parameter. This mechanism automatically up-weights loss terms that decrease slowly relative to their historical trend, promoting balanced optimization without manual tuning. The resulting adaptive weights  $\{\lambda_c(k)\}$  replace the fixed penalty weights  $\lambda_{\text{BC}}, \lambda_{\text{IC}}$  introduced in Eq. (5). When ReLoBRaLo is not activated, uniform weights  $\lambda_c = 1$  are used.

#### 2.5. Total Loss

Combining the curriculum-weighted PDE loss with the boundary and initial condition losses, the total training objective at iteration  $k$  is

$$\begin{aligned} \mathcal{L}_{\text{total}}(\theta; k) &= \lambda_{\text{PDE}}(k) \mathcal{L}_{\text{PDE}}^w(\theta) + \lambda_{\text{BC}}(k) \mathcal{L}_{\text{BC}}(\theta) \\ &\quad + \lambda_{\text{IC}}(k) \mathcal{L}_{\text{IC}}(\theta), \end{aligned} \quad (23)$$

where  $\mathcal{L}_{\text{BC}}$  and  $\mathcal{L}_{\text{IC}}$  are the standard MSE boundary and initial-condition losses:

$$\mathcal{L}_{\text{BC}}(\theta) = \frac{1}{N_{\partial\Omega}} \sum_{j=1}^{N_{\partial\Omega}} r_{\text{BC},j}^2, \quad \mathcal{L}_{\text{IC}}(\theta) = \frac{1}{N_{\text{IC}}} \sum_{l=1}^{N_{\text{IC}}} r_{\text{IC},l}^2, \quad (24)$$

and  $\lambda_{\text{PDE}}(k)$ ,  $\lambda_{\text{BC}}(k)$ ,  $\lambda_{\text{IC}}(k)$  are the ReLoBRaLo adaptive weights (or set to unity when ReLoBRaLo is not activated). At each iteration, the network evaluates PDE, boundary, and initial residuals via automatic differentiation; every  $k_{\text{upd}}$  iterations, the GMM is re-fitted to the current residuals and the sample weights  $\{w_i\}$  are updated according to the curriculum parameter  $\tau(k)$ . The parameters are then updated by a gradient-based optimizer (e.g., Adam followed by L-BFGS [44]). The framework is non-intrusive, requiring no modification to the PDE residual formulation or network architecture, and is applicable to both forward and inverse problems involving linear and nonlinear operators.

#### 2.6. Theoretical Properties of CGMPINN

We now establish the main theoretical properties of CGMPINN. The analysis targets the time-varying objective  $\mathcal{L}_{\text{total}}(\theta; k)$  under idealized full-batch gradient descent, so as to isolate the effect of the curriculum-guided GMM reweighting and the induced objective drift. The practical Adam→L-BFGS strategy is regarded as an effective solver for the same objective; a complete iterate-level theory for this hybrid optimizer is left for future work.

For the following results, we denote by  $\mathcal{L}_{\text{PDE}}(\theta) = \frac{1}{N_{\Omega}} \sum_{i=1}^{N_{\Omega}} r_{\text{PDE},i}^2$  the standard (unweighted) empirical PDE loss. In the convergence statement (Theorem 2.3),  $K$  denotes the iteration horizon of the gradient descent analysis (not the number of GMM components). In the generalization bound (Theorem 2.5),  $\rho$  denotes the data-generating distribution over  $\Omega \times [0, T]$  (not the ReLoBRaLo parameter from Section 2).

**Theorem 2.1** (Uniform equivalence between weighted and standard PDE losses). *Assume that the GMM variances satisfy  $0 < \underline{\sigma}^2 \leq \sigma_m^2 \leq \bar{\sigma}^2 < \infty$  for all mixture components. Then there exist constants  $0 < c_- \leq c_+ < \infty$ , depending only on  $\beta, \epsilon, N_{\Omega}, \underline{\sigma}^2$ , and  $\bar{\sigma}^2$ , such that for every  $\theta$ ,*

$$c_- \mathcal{L}_{\text{PDE}}(\theta) \leq \mathcal{L}_{\text{PDE}}^w(\theta) \leq c_+ \mathcal{L}_{\text{PDE}}(\theta). \quad (25)$$

*Hence, the curriculum-weighted PDE loss is uniformly equivalent to the standard empirical PDE residual loss, and optimization of  $\mathcal{L}_{\text{PDE}}^w(\theta)$  remains faithful to the original PDE objective up to uniform constants.*

*Remark 2.2.* Theorem 2.1 ensures that minimizing the curriculum-weighted objective  $\mathcal{L}_{\text{PDE}}^w(\theta)$  does not deviate from the original PDE residual minimization problem: any minimizer of the weighted loss is also an approximate minimizer of the standard loss, and vice versa.

**Theorem 2.3** (Sublinear convergence of the time-varying total loss). *Assume that, for each iteration  $k$ , the total loss  $\mathcal{L}_{\text{total}}(\theta; k)$  is  $L$ -smooth (i.e., its gradient is  $L$ -Lipschitz with Lipschitz constant  $L > 0$ ) and uniformly bounded from below, and that the inter-iteration drift induced by the curriculum update, GMM re-fitting, sample reweighting,*

and adaptive loss balancing is summable. Then, for the full-batch gradient descent iteration

$$\theta_{k+1} = \theta_k - \eta \nabla_{\theta} \mathcal{L}_{\text{total}}(\theta_k; k), \quad \eta \in (0, 1/L], \quad (26)$$

where  $\eta > 0$  denotes the step size, there exists a constant  $C > 0$ , independent of  $K$ , such that

$$\min_{0 \leq t \leq K} \|\nabla_{\theta} \mathcal{L}_{\text{total}}(\theta_t; t)\|^2 \leq \frac{C}{K+1}. \quad (27)$$

In particular,

$$\|\nabla_{\theta} \mathcal{L}_{\text{total}}(\theta_k; k)\| \rightarrow 0 \quad \text{as } k \rightarrow \infty. \quad (28)$$

**Remark 2.4.** Theorem 2.3 guarantees that, despite the time-varying nature of the CGMPINN objective (due to periodic GMM re-fitting, curriculum advancement, and adaptive loss balancing), gradient descent still converges to a stationary point at the standard  $O(1/K)$  rate, provided the cumulative objective drift remains controlled.

**Theorem 2.5** (Generalization bound for the weighted empirical PDE loss). *Under the proof-oriented split-sample construction described in Appendix A, assume that the PDE residual is uniformly bounded and that the induced weight function is bounded. Then, at a fixed refresh step and conditioned on the corresponding frozen weighting rule, with probability at least  $1 - \delta$ , the population weighted PDE risk satisfies*

$$\begin{aligned} \mathcal{E}_{\text{PDE}}^w(\theta) &\leq \mathcal{L}_{\text{PDE}}^w(\theta) + 2W \mathfrak{R}_{N_{\Omega}}(\mathcal{F}) \\ &\quad + 3BW \sqrt{\frac{\log(2/\delta)}{2N_{\Omega}}}, \end{aligned} \quad (29)$$

where  $\mathcal{F}$  denotes the squared-residual function class,  $B$  is the uniform residual bound,  $W \geq 1$  is the uniform weight bound (i.e.,  $0 \leq w_i \leq W$ ), and  $\mathfrak{R}_{N_{\Omega}}(\mathcal{F})$  is the Rademacher complexity of  $\mathcal{F}$ . Moreover, the original unweighted population risk obeys

$$\begin{aligned} \mathcal{E}_{\text{PDE}}(\theta) &\leq \mathcal{L}_{\text{PDE}}^w(\theta) + 2W \mathfrak{R}_{N_{\Omega}}(\mathcal{F}) \\ &\quad + 3BW \sqrt{\frac{\log(2/\delta)}{2N_{\Omega}}} + B \|w - 1\|_{L^1(\rho)}. \end{aligned} \quad (30)$$

Therefore, at a fixed refresh step, curriculum-based reweighting preserves statistical control of the induced weighted objective up to an explicit weighting-induced bias term relative to the original unweighted PDE risk.

**Remark 2.6.** Theorem 2.5 shows that the curriculum-weighted empirical loss generalizes to the population level at the standard rate, and the additional bias  $B \|w - 1\|_{L^1(\rho)}$  explicitly quantifies the cost of optimizing a reweighted surrogate instead of the original unweighted PDE risk.

**Remark 2.7** (PL-based refinement). Under an additional uniform Polyak–Łojasiewicz condition, the time-varying total loss admits a stronger PL-based convergence theory: the homogeneous part decays linearly, a drift-neighborhood estimate holds under uniformly bounded drift, and exact convergence to the common reference level follows when the objective drift is summable.

Detailed assumptions, explicit constants, and complete proofs of Theorems 2.1–2.5 and Remark 2.7 are deferred to Appendix A.

### 3. Numerical Experiments and Comparisons

This section systematically evaluates the proposed CGMPINN framework on a suite of benchmark PDEs spanning different types: elliptic (1D and 2D Poisson), parabolic (heat equation), hyperbolic (damped wave equation), advection-dominated (advection-diffusion equation), and nonlinear reaction-diffusion (Fisher-KPP equation). These problems are selected to cover a range of difficulties commonly encountered in practice, including high-gradient solutions, steep wavefronts, damped oscillatory dynamics, and nonlinear traveling waves.

For each benchmark, we first conduct an optimizer study comparing Adam, L-BFGS, and a two-stage Adam→L-BFGS strategy [44] within the CGMPINN framework, in order to identify the most effective training configuration. We then compare CGMPINN against five representative PINN variants: the canonical PINN [1], lbPINN [25], gPINN [27], LNN-PINN [28], and STAR-PINN [29]. All methods employ the same fully-connected neural network architecture as the solution approximator and are implemented in PyTorch to ensure a fair comparison. Note that in the PDE formulations below, problem-specific parameters (e.g.,  $\gamma$ ,  $\nu$ ,  $r$ ) refer to physical coefficients of the respective equations and should not be confused with the method parameters defined in Section 2.

In all benchmarks, the source term  $f$ , boundary data  $g$ , and initial conditions are determined by substituting the exact solution into the governing equation and the corresponding boundary/initial conditions.

The evaluation metrics are defined as follows: the final training loss  $e_{\text{Loss}} = \mathcal{L}_{\text{total}}(\theta^*)$ , the absolute  $L_2$  error  $e_2 = \|u - \hat{u}\|_2$ , the relative  $L_2$  error  $e_2/\|u\|_2$ , and the maximum absolute error  $e_{\infty} = \|u - \hat{u}\|_{\infty}$ , where  $\theta^*$  denotes the trained network parameters, and  $u$  and  $\hat{u}$  denote the exact and predicted solutions evaluated on the test points, respectively. Additionally, an ablation study comparing GMMPINN (GMM-based weighting only), CLPINN (curriculum learning only), and the full CGMPINN is conducted to disentangle the contributions of the individual components; the results are reported in Appendix B.

Table 1. Performance Comparison of Different Optimizers for Solving 1D Poisson Equation (with  $\alpha_1 = 5.0, \alpha_2 = 3.0, s = 20.0$ )

Optimizer	$e_{Loss}$	$e_2$	Relative $e_2$	$e_\infty$	CPU (s)
Adam	2.30e+1	1.70e+0	1.57e+0	2.93e+0	199.0
L-BFGS	<b>8.24e-4</b>	3.15e-4	2.91e-4	4.90e-4	1099.4
Adam→L-BFGS	9.60e-4	<b>1.96e-4</b>	<b>1.81e-4</b>	<b>3.74e-4</b>	895.9

Table 2. Performance Comparison of Different Methods for Solving 1D Poisson Equation (with  $\alpha_1 = 5.0, \alpha_2 = 3.0, s = 20.0$ )

Method	$e_{Loss}$	$e_2$	Relative $e_2$	$e_\infty$	CPU (s)
PINN	1.90e-3	8.83e-3	8.15e-3	9.19e-3	1018.2
lbPINN	2.95e+0	4.57e+0	4.22e+0	7.88e+0	1205.6
gPINN	1.02e-1	1.88e-2	1.74e-2	2.47e-2	5711.8
LNN-PINN	2.31e-3	4.50e-4	4.15e-4	7.89e-4	1422.0
STAR-PINN	6.87e-2	1.23e-3	1.14e-3	2.05e-3	1332.4
CGMPINN	<b>9.60e-4</b>	<b>1.96e-4</b>	<b>1.81e-4</b>	<b>3.74e-4</b>	895.9

### 3.1. 1D Poisson Equation

We begin with a 1D Poisson equation featuring a high-gradient analytical solution, which serves as a standard test for capturing sharp spatial variations. The problem is defined as

$$\begin{cases} u_{xx}(x) = f(x), & x \in \Omega, \\ u(x) = g(x), & x \in \partial\Omega, \end{cases} \quad (31)$$

with the analytical solution

$$u(x) = \sin(\alpha_1\pi x) \cos(\alpha_2\pi x) + \tanh(sx), \quad (32)$$

where  $\Omega = [0, 1]$ ,  $\alpha_1 = 5.0$ ,  $\alpha_2 = 3.0$ , and  $s = 20.0$  is the steepness parameter. The combination of multi-frequency sinusoidal components and a steep hyperbolic tangent transition makes this problem particularly challenging for neural network-based solvers. All methods in this subsection employ a four-hidden-layer network with 50 neurons per layer, trained on 1,500 randomly sampled interior collocation points and evaluated on 200 uniformly distributed test points.

Table 1 compares the three optimization strategies. The vanilla Adam optimizer fails to converge to an acceptable solution, producing errors several orders of magnitude larger than the two L-BFGS-based strategies. While pure L-BFGS achieves the lowest training loss ( $8.24 \times 10^{-4}$ ), the Adam→L-BFGS strategy yields the best generalization performance, reducing  $e_2$  by 37.8% and  $e_\infty$  by 23.7% compared to pure L-BFGS. Moreover, the two-stage strategy is 18.5% faster than pure L-BFGS, indicating that Adam pre-training provides a favorable initialization that accelerates subsequent L-BFGS convergence. The corresponding training loss curves and prediction results are shown in Figure 2. Based on these consistent findings, the Adam→L-BFGS strategy is adopted for all subsequent experiments.

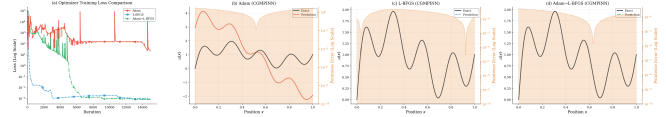


Figure 2. Optimizer comparison for 1D Poisson equation: (a) Training loss curves with different optimizers; (b)–(d) Predictions of CGMPINN with Adam, L-BFGS, and Adam→L-BFGS optimizers respectively, compared with the exact solution (the pointwise error in log scale is shown as the auxiliary y-axis).

Table 2 presents the comparison of CGMPINN against five baseline methods. CGMPINN achieves the best performance across all error metrics. In terms of  $e_2$ , CGMPINN attains  $1.96 \times 10^{-4}$ , representing a reduction of 97.8% relative to the canonical PINN ( $8.83 \times 10^{-3}$ ), 56.4% relative to LNN-PINN ( $4.50 \times 10^{-4}$ ), and 84.1% relative to STAR-PINN ( $1.23 \times 10^{-3}$ ). The  $e_\infty$  of CGMPINN ( $3.74 \times 10^{-4}$ ) is also the lowest among all methods, indicating uniformly accurate predictions across the domain. It is worth noting that lbPINN fails to converge for this problem, with errors exceeding those of the canonical PINN by orders of magnitude, and gPINN also underperforms the standard PINN despite incurring a  $5.6 \times$  higher computational cost. In contrast, CGMPINN achieves the best accuracy while maintaining the lowest CPU time among all methods, demonstrating that the curriculum-guided weighting mechanism improves accuracy without introducing significant computational overhead. The training loss curves and error distributions are further illustrated in Figure 3.

### 3.2. 2D Poisson Equation

To assess scalability to higher spatial dimensions, we consider a 2D Poisson equation on a rectangular domain with

Table 3. Performance Comparison of Different Optimizers for Solving 2D Poisson Equation (with  $\beta_1 = 3.0$ ,  $\beta_2 = 2.0$ )

Optimizer	$e_{\text{Loss}}$	$e_2$	Relative $e_2$	$e_\infty$	CPU (s)
Adam	$8.23e-2$	$3.97e-2$	$4.99e-2$	$2.46e-1$	441.4
L-BFGS	$3.93e-3$	$3.64e-3$	$4.56e-3$	$3.54e-2$	1914.7
Adam→L-BFGS	<b><math>7.78e-5</math></b>	<b><math>4.65e-4</math></b>	<b><math>5.83e-4</math></b>	<b><math>2.95e-3</math></b>	1453.2

 Table 4. Performance Comparison of Different Methods for Solving 2D Poisson Equation (with  $\beta_1 = 3.0$ ,  $\beta_2 = 2.0$ )

Method	$e_{\text{Loss}}$	$e_2$	Relative $e_2$	$e_\infty$	CPU (s)
PINN	$1.06e-4$	$1.08e-3$	$1.35e-3$	$7.28e-3$	1376.5
lbPINN	$2.03e-2$	$4.07e-3$	$5.11e-3$	$2.45e-2$	1509.5
gPINN	$2.41e-4$	$1.60e-3$	$2.01e-3$	$9.93e-3$	6876.9
LNN-PINN	$7.93e-5$	$8.12e-4$	$1.02e-3$	$9.36e-3$	2775.1
STAR-PINN	<b><math>7.30e-5</math></b>	$5.19e-4$	$6.51e-4$	$5.37e-3$	2339.2
CGMPINN	$7.78e-5$	<b><math>4.65e-4</math></b>	<b><math>5.83e-4</math></b>	<b><math>2.95e-3</math></b>	1453.2

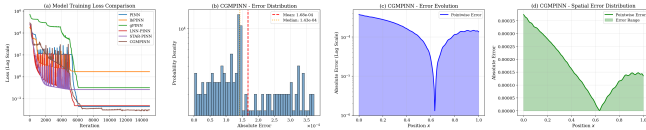


Figure 3. Performance comparison of different PINN variants for 1D Poisson equation: (a) Training loss curves of different models; (b) Absolute error probability density distribution of CGMPINN; (c) Pointwise error (log scale) of CGMPINN in the spatial domain; (d) Spatial absolute error distribution and error range of CGMPINN.

Dirichlet boundary conditions:

$$\begin{cases} u_{xx}(x, y) + u_{yy}(x, y) = f(x, y), & (x, y) \in \Omega, \\ u(x, y) = g(x, y), & (x, y) \in \partial\Omega, \end{cases} \quad (33)$$

with the analytical solution

$$u(x, y) = \sin(\beta_1 \pi x) \sin(\beta_2 \pi y) + e^{-x^2 - y^2}, \quad (34)$$

where  $\Omega = [0, 1]^2$ ,  $\beta_1 = 3.0$  and  $\beta_2 = 2.0$ . The multi-frequency oscillations coupled with a localized Gaussian component introduce anisotropic gradients in both spatial directions. All methods in this subsection use a four-hidden-layer network with 50 neurons per layer, trained on 2,000 randomly sampled interior collocation points and 250 boundary points, and evaluated on 10,000 uniformly distributed test points.

Table 3 reports the optimizer comparison results. Consistent with the 1D case, the Adam→L-BFGS strategy achieves the best performance across all metrics. Compared to pure L-BFGS, it reduces  $e_{\text{Loss}}$  by 98.0%,  $e_2$  by 87.2%, and  $e_\infty$  by 91.7%, while also reducing the training time by 24.1%. The Adam optimizer again shows limited convergence capability, with errors approximately one order of magnitude higher

than the L-BFGS-based strategies. The training loss curves and prediction results are shown in Figure 4.

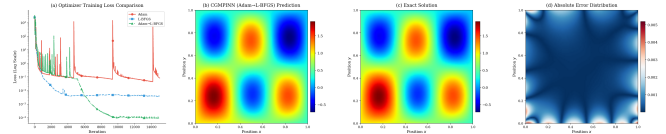


Figure 4. Optimizer comparison for 2D Poisson equation: (a) Training loss curves of different optimizers; (b) Prediction result of CGMPINN with Adam→L-BFGS optimizer; (c) Exact solution of the equation; (d) Absolute error distribution of the prediction.

Table 4 compares CGMPINN with five baseline methods on the 2D Poisson equation. From the perspective of computational efficiency, CGMPINN achieves a favorable trade-off between runtime and solution quality. Its training cost is 1453.2 s, which is close to that of the standard PINN (1376.5 s) and substantially lower than those of LNN-PINN (2775.1 s), STAR-PINN (2339.2 s), and especially gPINN (6876.9 s). Despite this relatively low computational cost, CGMPINN still attains the best accuracy among all compared methods, yielding the lowest values of  $e_2$  ( $4.65 \times 10^{-4}$ ), relative  $e_2$  ( $5.83 \times 10^{-4}$ ), and  $e_\infty$  ( $2.95 \times 10^{-3}$ ). In particular, compared with the standard PINN, CGMPINN reduces  $e_2$  by 56.9% and  $e_\infty$  by 59.5%; compared with STAR-PINN, it further improves  $e_2$  and  $e_\infty$  by 10.4% and 45.1%, respectively. Although CGMPINN does not achieve the minimum training loss, its  $e_{\text{Loss}}$  remains comparable to that of STAR-PINN. Overall, these results suggest that CGMPINN achieves a more favorable balance between computational efficiency and predictive accuracy on this benchmark, while also demonstrating its effectiveness in multi-dimensional settings. The training loss curves and error distributions are further illustrated in Figure 5.

Table 5. Performance Comparison of Different Optimizers for Solving Heat Equation (with  $\alpha_1 = 1.0, \alpha_2 = 2.0, s = 10.0$ )

Optimizer	$e_{\text{Loss}}$	$e_2$	Relative $e_2$	$e_\infty$	CPU (s)
Adam	$1.38e-2$	$1.63e-2$	$1.43e-2$	$1.21e-1$	292.9
L-BFGS	$8.69e-5$	$1.18e-3$	$1.03e-3$	$7.63e-3$	1517.3
Adam→L-BFGS	<b><math>1.53e-5</math></b>	<b><math>4.04e-4</math></b>	<b><math>3.54e-4</math></b>	<b><math>2.86e-3</math></b>	1430.0

Table 6. Performance Comparison of Different Methods for Solving Heat Equation (with  $\alpha_1 = 1.0, \alpha_2 = 2.0, s = 10.0$ )

Method	$e_{\text{Loss}}$	$e_2$	Relative $e_2$	$e_\infty$	CPU (s)
PINN	$3.59e-5$	$1.46e-3$	$1.28e-3$	$1.93e-2$	1342.8
lbPINN	$1.58e-2$	$3.22e-3$	$2.83e-3$	$3.44e-2$	1134.1
gPINN	$1.56e-4$	$3.11e-3$	$2.73e-3$	$3.41e-2$	5331.7
LNN-PINN	$3.09e-5$	$9.57e-4$	$8.39e-4$	$1.08e-2$	2333.2
STAR-PINN	$9.96e-5$	$1.63e-3$	$1.43e-3$	$1.88e-2$	1776.6
CGMPINN	<b><math>1.53e-5</math></b>	<b><math>4.04e-4</math></b>	<b><math>3.54e-4</math></b>	<b><math>2.86e-3</math></b>	1430.0

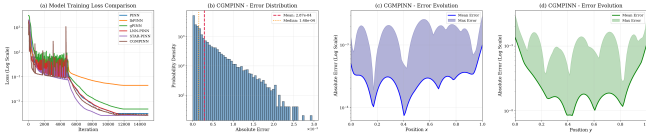


Figure 5. Performance comparison of different PINN variants for 2D Poisson equation: (a) Training loss curves of different models; (b) Absolute error probability density distribution of CGMPINN; (c) Mean and max absolute error of CGMPINN in the x spatial direction; (d) Mean and max absolute error of CGMPINN in the y spatial direction.

### 3.3. Heat Equation

We next consider a time-dependent parabolic problem: the 1D heat equation with a localized steep gradient induced by a hyperbolic tangent term. The problem reads

$$\begin{cases} u_t(x, t) = u_{xx}(x, t) + f(x, t), & (x, t) \in \Omega \times [0, 1], \\ u(x, 0) = u_0(x), & x \in \Omega, \\ u(x, t) = g(x, t), & (x, t) \in \partial\Omega \times [0, 1], \end{cases} \quad (35)$$

with the analytical solution

$$u(x, t) = (\sin(\alpha_1\pi x) + \tanh(sx)) \sin(\alpha_2\pi t), \quad (36)$$

where  $\Omega = [0, 1]$ ,  $\alpha_1 = 1.0$ ,  $\alpha_2 = 2.0$ , and  $s = 10.0$ . The temporal oscillation modulated by a spatially localized steep gradient tests the ability of neural solvers to resolve both temporal dynamics and spatial fine structure simultaneously. All methods in this subsection employ a four-hidden-layer network with 50 neurons per layer, trained on 1,500 randomly sampled interior collocation points, 300 boundary points, and 300 initial condition points, and evaluated on 10,000 uniformly distributed test points.

Table 5 reports the optimizer comparison. The Adam→L-BFGS strategy again achieves the best results across all met-

rics, reducing  $e_{\text{Loss}}$  by 82.4% and  $e_2$  by 65.8% compared to pure L-BFGS, while requiring 5.8% less training time. The Adam optimizer yields errors more than an order of magnitude higher than the L-BFGS-based strategies, consistent with observations on the Poisson problems. The training loss curves and prediction results are shown in Figure 6.

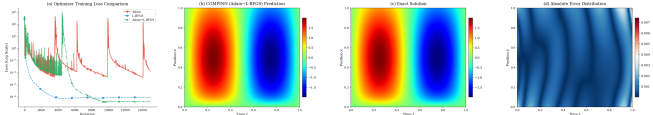


Figure 6. Optimizer comparison for 1D heat equation: (a) Training loss curves of different optimizers; (b) Prediction result of CGMPINN with Adam→L-BFGS optimizer; (c) Exact solution of the equation; (d) Absolute error distribution of the prediction.

Table 6 compares CGMPINN with five baseline methods on the heat equation. CGMPINN achieves the best accuracy among all compared methods, attaining the lowest values of  $e_2$ , relative  $e_2$ , and  $e_\infty$ . In particular, its  $e_2$  is  $4.04 \times 10^{-4}$ , corresponding to reductions of 72.3% and 57.8% relative to the standard PINN and LNN-PINN, respectively. The smallest  $e_\infty$  ( $2.86 \times 10^{-3}$ ) further indicates that CGMPINN provides more uniformly accurate predictions, with reductions of 85.2% and 73.5% compared with the standard PINN and LNN-PINN, respectively. In addition, CGMPINN also attains the lowest training loss ( $1.53 \times 10^{-5}$ ), suggesting more effective optimization on this benchmark. Although its CPU time (1430.0 s) is slightly higher than that of the standard PINN (1342.8 s), it remains substantially lower than those of LNN-PINN (2333.2 s), STAR-PINN (1776.6 s), and gPINN (5331.7 s). Overall, these results indicate that CGMPINN achieves a favorable balance between predictive accuracy and computational cost on this benchmark. The training loss curves and error distributions are further illustrated in Figure 7.

Table 7. Performance Comparison of Different Optimizers for Solving Damped Wave Equation (with  $\alpha_1 = 1.0$ ,  $\alpha_2 = 1.0$ ,  $\gamma = 0.1$ )

Optimizer	$e_{\text{Loss}}$	$e_2$	Relative $e_2$	$e_\infty$	CPU (s)
Adam	$1.81e-4$	$4.59e-3$	$9.64e-3$	$1.50e-2$	535.7
L-BFGS	$1.33e-5$	$1.18e-3$	$2.49e-3$	$6.11e-3$	2486.0
Adam→L-BFGS	<b><math>1.66e-6</math></b>	<b><math>3.37e-4</math></b>	<b><math>7.07e-4</math></b>	<b><math>2.20e-3</math></b>	678.0

 Table 8. Performance Comparison of Different Methods for Solving Damped Wave Equation (with  $\alpha_1 = 1.0$ ,  $\alpha_2 = 1.0$ ,  $\gamma = 0.1$ )

Method	$e_{\text{Loss}}$	$e_2$	Relative $e_2$	$e_\infty$	CPU (s)
PINN	$1.17e-5$	$1.14e-3$	$2.40e-3$	$3.81e-3$	718.2
lbPINN	$1.62e-3$	$4.65e-4$	$9.76e-4$	$3.48e-3$	1881.3
gPINN	$7.74e-6$	$9.48e-4$	$1.99e-3$	$3.00e-3$	2971.8
LNN-PINN	<b><math>1.54e-6</math></b>	$4.66e-4$	$9.79e-4$	$2.30e-3$	1164.5
STAR-PINN	$3.22e-5$	$2.53e-3$	$5.31e-3$	$7.14e-3$	916.4
CGMPINN	$1.66e-6$	<b><math>3.37e-4</math></b>	<b><math>7.07e-4</math></b>	<b><math>2.20e-3</math></b>	678.0

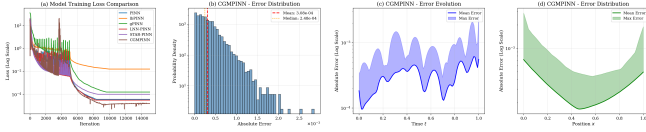


Figure 7. Performance comparison of different PINN variants for 1D heat equation: (a) Training loss curves of different models; (b) Absolute error probability density distribution of CGMPINN; (c) Temporal evolution of the mean and max absolute error of CGMPINN; (d) Mean and max absolute error of CGMPINN in the  $x$  spatial direction.

### 3.4. Damped Wave Equation

We proceed to a second-order hyperbolic problem: the 1D damped wave equation, which models wave propagation with energy dissipation. The governing equation is

$$\begin{cases} u_{tt} + 2\gamma u_t - c^2 u_{xx} = 0, & (x, t) \in \Omega \times [0, 1], \\ u(x, 0) = u_0(x), & x \in \Omega, \\ u_t(x, 0) = v_0(x), & x \in \Omega, \\ u(x, t) = g(x, t), & (x, t) \in \partial\Omega \times [0, 1], \end{cases} \quad (37)$$

where  $\Omega = [0, 1]$ ,  $\gamma > 0$  is the damping coefficient,  $c$  is the wave speed, and  $u_0(x)$  and  $v_0(x)$  denote the initial displacement and velocity profiles, respectively. The analytical solution is

$$u(x, t) = e^{-\gamma t} \sin(\alpha_1 \pi x) \cos(\alpha_2 \pi t), \quad (38)$$

with  $c = \sqrt{\gamma^2 + (\alpha_2 \pi)^2} / (\alpha_1 \pi)$ , and parameters  $\alpha_1 = 1.0$ ,  $\alpha_2 = 1.0$ ,  $\gamma = 0.1$ . The exponentially decaying oscillatory behavior requires the solver to accurately resolve both the spatial modal structure and the temporal amplitude decay. All methods in this subsection employ a four-hidden-layer network with 50 neurons per layer, trained on 2,000 randomly sampled interior collocation points, 300 boundary

points, and 300 initial condition points, and evaluated on 10,000 uniformly distributed test points.

Table 7 shows the optimizer comparison. The Adam→L-BFGS strategy delivers the most pronounced advantage on this problem, reducing  $e_{\text{Loss}}$  by 87.5%,  $e_2$  by 71.4%, and  $e_\infty$  by 64.0% relative to pure L-BFGS, while requiring only 27.3% of the L-BFGS training time. This significant efficiency gain suggests that for second-order time-dependent PDEs, Adam pre-training is especially effective at navigating the loss landscape toward a basin of attraction that L-BFGS can efficiently exploit. The corresponding training loss curves and prediction results are shown in Figure 8.

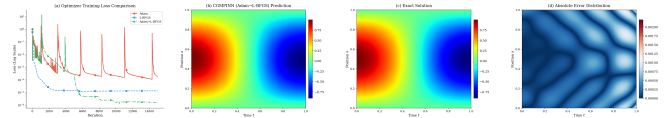


Figure 8. Optimizer comparison for 1D damped wave equation: (a) Training loss curves of different optimizers; (b) Prediction result of CGMPINN with Adam→L-BFGS optimizer; (c) Exact solution of the equation; (d) Absolute error distribution of the prediction.

Table 8 compares CGMPINN with five baseline methods on the damped wave equation. From the perspective of computational efficiency, CGMPINN is the most cost-effective method, requiring only 678.0 s of CPU time, which is the lowest among all compared methods. This corresponds to reductions of 5.6%, 41.8%, and 77.2% relative to the standard PINN, LNN-PINN, and gPINN, respectively. Despite this lower runtime, CGMPINN still achieves the best accuracy, attaining the lowest values of  $e_2$ , relative  $e_2$ , and  $e_\infty$ . In particular, compared with the standard PINN, its  $e_2$  is reduced by 70.4%; compared with the best-performing baseline methods in terms of  $e_2$ , namely lbPINN and LNN-PINN, the reductions are 27.5% and 27.7%, respectively. Its training loss is also very close to the minimum achieved by

Table 9. Performance Comparison of Different Optimizers for Solving Advection-Diffusion Equation (with  $a = 1.0, \nu = 10^{-2}$ )

Optimizer	$e_{\text{Loss}}$	$e_2$	Relative $e_2$	$e_\infty$	CPU (s)
Adam	$2.44e-4$	$7.35e-3$	$1.09e-2$	$1.33e-2$	434.7
L-BFGS	$1.84e-6$	$5.27e-4$	$7.82e-4$	$1.33e-3$	512.2
Adam→L-BFGS	<b><math>1.54e-6</math></b>	<b><math>2.57e-4</math></b>	<b><math>3.82e-4</math></b>	<b><math>7.14e-4</math></b>	532.4

 Table 10. Performance Comparison of Different Methods for Solving Advection-Diffusion Equation (with  $a = 1.0, \nu = 10^{-2}$ )

Method	$e_{\text{Loss}}$	$e_2$	Relative $e_2$	$e_\infty$	CPU (s)
PINN	$4.28e-6$	$7.14e-4$	$1.06e-3$	$2.07e-3$	446.6
lbPINN	$2.76e-3$	$4.44e-4$	$6.60e-4$	$1.16e-3$	2018.2
gPINN	$5.48e-6$	$5.69e-4$	$8.44e-4$	$1.35e-3$	1885.6
LNN-PINN	$1.66e-5$	$7.97e-4$	$1.18e-3$	$2.79e-3$	678.6
STAR-PINN	$3.56e-6$	$4.41e-4$	$6.55e-4$	$1.57e-3$	623.6
CGMPINN	<b><math>1.54e-6</math></b>	<b><math>2.57e-4</math></b>	<b><math>3.82e-4</math></b>	<b><math>7.14e-4</math></b>	532.4

LNN-PINN. These results suggest that CGMPINN achieves a highly favorable balance between computational efficiency and predictive accuracy on this benchmark. The training loss curves, spatial-temporal prediction profiles, and point-wise error analysis are further illustrated in Figure 9.

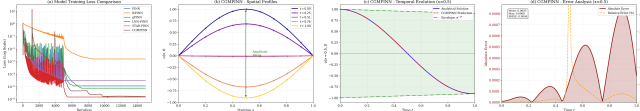


Figure 9. Performance comparison of different PINN variants for 1D damped wave equation: (a) Training loss curves of different models; (b) Spatial profiles of CGMPINN prediction at different time steps; (c) Temporal evolution of CGMPINN prediction at  $x = 0.5$  compared with the analytical solution; (d) Absolute and relative error of CGMPINN at  $x = 0.5$ .

### 3.5. Advection-Diffusion Equation

We consider a 1D advection-diffusion equation in the advection-dominated regime, a well-known challenging benchmark for PINNs due to the steep traveling wavefront that induces spectral bias and optimization instability. The governing equation with periodic boundary conditions is

$$\begin{cases} u_t + a u_x - \nu u_{xx} = 0, & (x, t) \in \Omega \times [0, 1], \\ u(x, 0) = \sin(\pi x), & x \in \Omega, \\ u(-1, t) = u(1, t), \quad u_x(-1, t) = u_x(1, t), & t \in [0, 1], \end{cases} \quad (39)$$

with the exact solution

$$u(x, t) = e^{-\nu\pi^2 t} \sin(\pi(x - at)), \quad (40)$$

where  $\Omega = [-1, 1]$ ,  $a = 1.0$  is the advection coefficient, and  $\nu = 10^{-2}$  is the diffusion coefficient. All methods in this subsection employ a four-hidden-layer network with 50 neurons per layer, trained on 3,000 randomly sampled

interior collocation points, 300 boundary points, and 300 initial condition points, and evaluated on 10,000 uniformly distributed test points.

The optimizer comparison in Table 9 shows that the Adam→L-BFGS strategy outperforms the alternatives, reducing  $e_2$  by 51.2% and  $e_\infty$  by 46.3% relative to pure L-BFGS, with a comparable training time. The performance gap between L-BFGS and Adam→L-BFGS is narrower for this problem than for the previous benchmarks, suggesting that L-BFGS alone is relatively effective for the advection-diffusion dynamics, though Adam pre-training still provides a measurable benefit. The training loss curves and prediction results are shown in Figure 10.

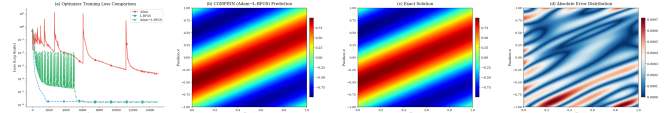


Figure 10. Optimizer comparison for 1D advection-diffusion equation: (a) Training loss curves of different optimizers; (b) Prediction result of CGMPINN with Adam→L-BFGS optimizer; (c) Exact solution of the equation; (d) Absolute error distribution of the prediction.

Table 10 compares the performance of CGMPINN with five baseline methods on the advection-diffusion equation. CGMPINN delivers the best accuracy, achieving the lowest values of  $e_2$ , relative  $e_2$ , and  $e_\infty$  among all methods. Specifically, its  $e_2$  is  $2.57 \times 10^{-4}$ , corresponding to reductions of 64.0%, 42.1%, and 41.7% relative to the standard PINN, lbPINN, and STAR-PINN, respectively. Its  $e_\infty$  is also the smallest at  $7.14 \times 10^{-4}$ , indicating more uniformly accurate predictions across the domain and a 65.5% reduction compared with the standard PINN. Moreover, CGMPINN attains the lowest training loss ( $1.54 \times 10^{-6}$ ), suggesting effective optimization on this benchmark. Although its CPU

Table 11. Performance Comparison of Different Optimizers for Solving Fisher-KPP Equation (with  $D = 0.25$ ,  $r = 4.0$ )

Optimizer	$e_{\text{Loss}}$	$e_2$	Relative $e_2$	$e_\infty$	CPU (s)
Adam	$4.11e-5$	$1.40e-3$	$1.82e-3$	$5.38e-3$	1319.9
L-BFGS	$9.33e-7$	$1.62e-3$	$2.11e-3$	$5.87e-3$	1526.9
Adam→L-BFGS	<b><math>3.62e-7</math></b>	<b><math>7.64e-4</math></b>	<b><math>9.94e-4</math></b>	<b><math>4.00e-3</math></b>	1722.9

 Table 12. Performance Comparison of Different Methods for Solving Fisher-KPP Equation (with  $D = 0.25$ ,  $r = 4.0$ )

Method	$e_{\text{Loss}}$	$e_2$	Relative $e_2$	$e_\infty$	CPU (s)
PINN	$3.52e-6$	$1.65e-3$	$2.14e-3$	$6.46e-3$	1527.0
lbPINN	$3.57e-4$	$1.14e-3$	$1.48e-3$	$5.81e-3$	5711.2
gPINN	$3.45e-6$	$1.72e-3$	$2.24e-3$	$7.03e-3$	7647.0
LNN-PINN	$1.62e-6$	$4.66e-3$	$6.06e-3$	$2.14e-2$	2823.3
STAR-PINN	$7.23e-6$	$1.10e-3$	$1.43e-3$	$7.38e-3$	1698.6
CGMPINN	<b><math>3.62e-7</math></b>	<b><math>7.64e-4</math></b>	<b><math>9.94e-4</math></b>	<b><math>4.00e-3</math></b>	1722.9

time (532.4 s) is slightly higher than that of the standard PINN (446.6 s), it remains substantially lower than those of lbPINN (2018.2 s) and gPINN (1885.6 s), demonstrating that the accuracy gains are obtained with only modest additional computational cost. The training loss curves and error distributions are further illustrated in Figure 11.

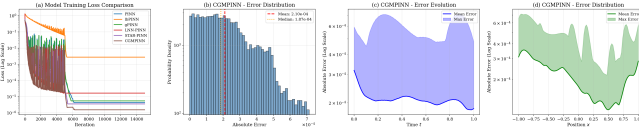


Figure 11. Performance comparison of different PINN variants for 1D advection-diffusion equation: (a) Training loss curves of different models; (b) Absolute error probability density distribution of CGMPINN; (c) Temporal evolution of the mean and max absolute error of CGMPINN; (d) Mean and max absolute error of CGMPINN in the  $x$  spatial direction.

As illustrated in Figure 12, the temporal derivative  $u_t$  is predominantly balanced by the advection term  $-au_x$  across the spatial domain at  $t = 0.25, 0.5$ , and  $0.75$ , while the diffusion contribution  $\nu u_{xx}$  remains an order of magnitude smaller, confirming the advection-dominated regime of this problem. The PDE residual is consistently bounded at the  $\mathcal{O}(10^{-3})$  level over all examined time instants, indicating that the learned solution satisfies the governing equation with high fidelity throughout the temporal domain.

### 3.6. Fisher-KPP Equation

Finally, we evaluate CGMPINN on the Fisher-KPP equation, a nonlinear reaction-diffusion PDE that admits traveling wave solutions with steep fronts. The strong coupling between the nonlinear reaction and diffusion terms makes this problem a demanding test case. The governing equation

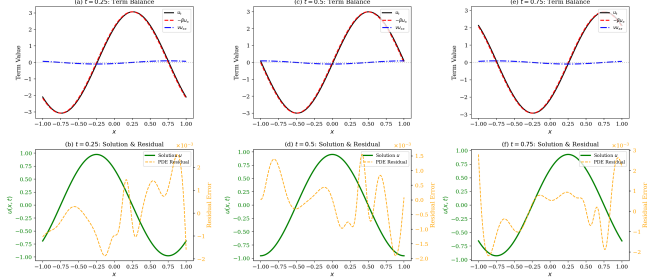


Figure 12. Term balance, solution and residual visualization for 1D advection-diffusion equation: (a)(c)(e) Balance of temporal derivative, advection and diffusion terms at  $t = 0.25, t = 0.5$  and  $t = 0.75$ ; (b)(d)(f) Predicted solution and PDE residual distribution at the corresponding time steps.

is

$$\begin{cases} u_t = D u_{xx} + r u(1 - u), & (x, t) \in \Omega \times [0, 2], \\ u(x, 0) = u_0(x), & x \in \Omega, \\ u(x, t) = g(x, t), & (x, t) \in \partial\Omega \times [0, 2], \end{cases} \quad (41)$$

with the Ablowitz–Zepetella exact traveling wave solution

$$u(x, t) = \frac{1}{(1 + \exp(\lambda(x - ct)))^2}, \quad (42)$$

where the waveform steepness parameter and wave speed are determined by

$$\lambda = \sqrt{\frac{r}{6D}}, \quad c = 5\sqrt{\frac{Dr}{6}}. \quad (43)$$

We set  $\Omega = [-5, 5]$ , diffusion coefficient  $D = 0.25$ , and growth rate  $r = 4.0$ . Owing to the stronger nonlinearity of this equation compared with the previous cases, all methods in this subsection adopt a moderately enlarged network with

four hidden layers of 80 neurons each, trained on 8,000 randomly sampled interior collocation points, 400 boundary points, and 400 initial condition points, and evaluated on 10,000 uniformly distributed test points.

Table 11 presents the optimizer comparison. The Adam→L-BFGS strategy yields the best performance, reducing  $e_{\text{Loss}}$  by 61.2% and  $e_2$  by 52.8% compared to pure L-BFGS. An interesting observation is that the pure L-BFGS optimizer produces a higher  $e_2$  ( $1.62 \times 10^{-3}$ ) than the Adam optimizer ( $1.40 \times 10^{-3}$ ) despite achieving a lower training loss, suggesting that L-BFGS converges to a sharper minimum that does not generalize as well on this nonlinear problem. The two-stage strategy mitigates this issue by leveraging the broader exploration of Adam before the local refinement of L-BFGS. The training loss curves and prediction results are shown in Figure 13.

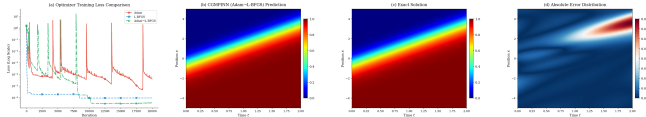


Figure 13. Optimizer comparison for 1D Fisher-KPP equation: (a) Training loss curves of different optimizers; (b) Prediction result of CGMPINN with Adam→L-BFGS optimizer; (c) Exact solution of the equation; (d) Absolute error distribution of the prediction.

Table 12 summarizes the performance comparison among the considered methods. CGMPINN achieves the best results across all reported metrics, with  $e_2 = 7.64 \times 10^{-4}$  and  $e_\infty = 4.00 \times 10^{-3}$ . Compared with the canonical PINN ( $e_2 = 1.65 \times 10^{-3}$ ), CGMPINN reduces  $e_2$  by 53.7%. The second-best method in terms of  $e_2$  is STAR-PINN ( $1.10 \times 10^{-3}$ ), which is still outperformed by CGMPINN by 30.5%. Notably, LNN-PINN ( $e_2 = 4.66 \times 10^{-3}$ ) fails to accurately capture the traveling-wave solution for this nonlinear problem, yielding an error nearly three times larger than that of the canonical PINN despite attaining a lower training loss. This discrepancy between training loss and test accuracy reflects the challenge of optimizing PINNs for nonlinear PDEs with steep fronts. Among the remaining baselines, lbPINN and gPINN achieve only modest improvements in  $e_2$  over the canonical PINN, at the expense of  $3.7\times$  and  $5.0\times$  higher training costs, respectively. By contrast, CGMPINN requires only 1722.9 s, representing a 12.8% increase over the standard PINN, while delivering the best overall accuracy and robustly capturing both the wave speed and the front profile. The training loss curves, wavefront tracking, and wave speed estimation results are further illustrated in Figure 14.

As shown in Figure 15, the temporal derivative  $u_t$  is nearly entirely balanced by the reaction term  $ru(1-u)$  across the spatial domain at  $t = 0.5, 1.0$ , and  $1.5$ , whereas the diffusion contribution  $Du_{xx}$  is comparatively negligible, confirming the reaction-dominated nature of the Fisher-KPP

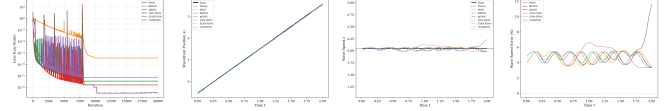


Figure 14. Performance comparison of different PINN variants for 1D Fisher-KPP equation: (a) Training loss curves of different models; (b) Wavefront tracking results of different PINN models; (c) Wave speed estimation results of different PINN models; (d) Temporal evolution of wave speed relative error for different models.

dynamics during front propagation. The PDE residual remains at the  $\mathcal{O}(10^{-3})$ – $\mathcal{O}(10^{-4})$  level over all examined time instants and decreases monotonically as time progresses, demonstrating that the predicted solution satisfies the governing equation with high accuracy throughout the temporal evolution.

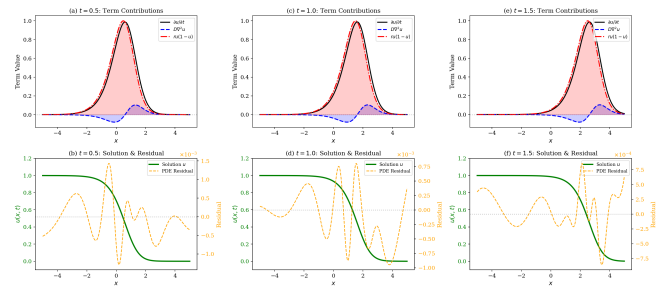


Figure 15. Term contribution, solution and residual visualization for 1D Fisher-KPP equation: (a)(c)(e) PDE term contributions at  $t = 0.5, t = 1.0$  and  $t = 1.5$ ; (b)(d)(f) Predicted solution and PDE residual distribution at the corresponding time steps.

## 4. Conclusion and Future Work

In this paper, we proposed CGMPINN, a curriculum-guided physics-informed neural network framework that integrates Gaussian mixture modeling with dynamic curriculum learning for solving partial differential equations. The core idea is to employ a GMM to statistically characterize the distribution of PDE residuals, thereby providing a principled, data-driven quantification of local learning difficulty. A smooth curriculum schedule then progressively transitions training focus from easy, well-conditioned regions to hard, uncertain ones, while a precision-based variance modulation mechanism further prioritizes reliable clusters during early training. This dual curriculum is unified through a shared curriculum parameter and optionally coupled with ReLoBRaLo-based self-adaptive loss balancing. Systematic evaluations on six benchmark PDEs demonstrate that CGMPINN consistently achieves the lowest  $e_2$  and  $e_\infty$  errors among all compared methods, with reductions of up to 97.8% in  $e_2$  relative to the canonical PINN. Notably, these accuracy gains incur no significant computational overhead. On the theoretical front, we established

formal guarantees for the proposed framework, including uniform equivalence between the curriculum-weighted and standard PDE losses, sublinear convergence of the gradient norm, and a generalization bound with an explicit weighting-induced bias characterization, thereby providing principled justification for the curriculum-guided reweighting strategy. An ablation study further confirms that the two core components—GMM-based difficulty quantification and curriculum scheduling—are complementary: neither component alone matches the performance of their combination, and omitting the curriculum schedule can lead to optimization failure on challenging problems.

Despite the encouraging results, several directions merit further investigation. The current experiments are restricted to one- and two-dimensional domains; extending CGMPINN to high-dimensional PDEs and assessing the scalability of GMM-based difficulty quantification in such settings is an important next step. Developing principled strategies for automatic selection of the number of mixture components  $K$  and the update frequency  $k_{\text{upd}}$ , for instance via information-theoretic criteria, would further reduce manual tuning. Combining the curriculum-guided mechanism with domain decomposition approaches and extending the framework to inverse problems with sparse, noisy observations are also natural generalizations. On the theoretical side, the present analysis establishes convergence, loss equivalence, and generalization guarantees under idealized full-batch gradient dynamics; extending these results to a complete iterate-level convergence theory for the practical Adam→L-BFGS training scheme and establishing tighter bounds that formally certify the advantage of dynamic curriculum reweighting over standard PINNs remain valuable open directions.

## References

- [1] Maziar Raissi, Paris Perdikaris, and George Emmanouil Karniadakis. Physics-informed neural networks: A deep learning framework for solving forward and inverse problems involving nonlinear partial differential equations. *Journal of Computational Physics*, 378:686–707, 2019.
- [2] George Emmanouil Karniadakis, Ioannis George Kevrekidis, Lu Lu, Paris Perdikaris, Sifan Wang, and Liu Yang. Physics-informed machine learning. *Nature Reviews Physics*, 3(6):422–440, 2021.
- [3] Olgierd Cecil Zienkiewicz. *The Finite Element Method*. McGraw-Hill, London; New York, 3rd edition, 1977.
- [4] Bengt Fornberg. *A Practical Guide to Pseudospectral Methods*. Cambridge Monographs on Applied and Computational Mathematics. Cambridge University Press, Cambridge, 1996.
- [5] Jiequn Han, Arnulf Jentzen, and Weinan E. Solving high-dimensional partial differential equations using deep learning. *Proceedings of the National Academy of Sciences of the United States of America*, 115(34):8505–8510, 2018.
- [6] Justin Sirignano and Konstantinos Spiliopoulos. DGM: A deep learning algorithm for solving partial differential equations. *Journal of Computational Physics*, 375:1339–1364, 2018.
- [7] Isaac Elias Lagaris, Aristidis Likas, and Dimitrios Ioannis Fotiadis. Artificial neural networks for solving ordinary and partial differential equations. *IEEE Transactions on Neural Networks*, 9(5):987–1000, 1998.
- [8] M. W. M. Gamini Dissanayake and Nhan Phan-Thien. Neural-network-based approximations for solving partial differential equations. *Communications in Numerical Methods in Engineering*, 10(3):195–201, 1994.
- [9] Tengmao Yang, Zhihao Qian, Nianzhi Hang, and Moubin Liu. S-PINN: Stabilized physics-informed neural networks for alleviating barriers between multi-level co-optimization. *Computer Methods in Applied Mechanics and Engineering*, 447:118348, 2025.
- [10] Zhaoyang Zhang and Qingwang Wang. allaPINNs: A physics-informed neural network with improvement of information representation and loss optimization for solving partial differential equations. *Acta Physica Sinica*, 74(18):188701, 2025.
- [11] Maziar Raissi, Alireza Yazdani, and George Emmanouil Karniadakis. Hidden fluid mechanics: Learning velocity and pressure fields from flow visualizations. *Science*, 367(6481):1026–1030, 2020.
- [12] Francisco Sahli Costabal, Yibo Yang, Paris Perdikaris, Daniel Hurtado, and Ellen Kuhl. Physics-informed neural networks for cardiac activation mapping. *Frontiers in Physics*, 8:42, 2020.
- [13] Kazuya Ishitsuka, Keiichi Ishizu, Norihiro Watanabe, Yusuke Yamaya, Anna Suzuki, Toshiyuki Bandai, Yusuke Ohta, Toru Mogi, Hiroshi Asanuma, Takuya Kajiwara, and Takeshi Sugimoto. Reliable and practical inverse modeling of natural-state geothermal systems using physics-informed neural networks: Three-dimensional model construction and assimilation with magnetotelluric data. *Journal of Geophysical Research: Machine Learning and Computation*, 2:e2025JH000683, 2025.

- [14] Yuyao Chen, Lu Lu, George Emmanouil Karniadakis, and Luca Dal Negro. Physics-informed neural networks for inverse problems in nano-optics and meta-materials. *Optics Express*, 28(8):11618, 2020.
- [15] Salvatore Cuomo, Vincenzo Schiano Di Cola, Fabio Giampaolo, Gianluigi Rozza, Maziar Raissi, and Francesco Piccialli. Scientific machine learning through physics-informed neural networks: Where we are and what’s next. *Journal of Scientific Computing*, 92(3):88, 2022.
- [16] Sifan Wang, Yujun Teng, and Paris Perdikaris. Understanding and mitigating gradient flow pathologies in physics-informed neural networks. *SIAM Journal on Scientific Computing*, 43(5):A3055–A3081, 2021.
- [17] Sifan Wang, Xinling Yu, and Paris Perdikaris. When and why PINNs fail to train: A neural tangent kernel perspective. *Journal of Computational Physics*, 449:110768, 2022.
- [18] Aditi Krishnapriyan, Amir Gholami, Shandian Zhe, Robert Martin Kirby, and Michael Warren Mahoney. Characterizing possible failure modes in physics-informed neural networks. In *Advances in Neural Information Processing Systems*, volume 34, pages 26548–26560, 2021.
- [19] Olga Fuks and Hamdi Tchelepi. Limitations of physics informed machine learning for nonlinear two-phase transport in porous media. *Journal of Machine Learning for Modeling and Computing*, 1(1):19–37, 2020.
- [20] Nasim Rahaman, Aristide Baratin, Devansh Arpit, Felix Dräxler, Min Lin, Fred A. Hamprecht, Yoshua Bengio, and Aaron Courville. On the spectral bias of neural networks. In *Proceedings of the 36th International Conference on Machine Learning, ICML ’19*, pages 5301–5310, 2019.
- [21] Zhi-Qin John Xu, Yaoyu Zhang, Tao Luo, Yanyang Xiao, and Zheng Ma. Frequency principle: Fourier analysis sheds light on deep neural networks. *Communications in Computational Physics*, 28(5):1746–1767, 2020.
- [22] Arka Daw, Jie Bu, Sifan Wang, Paris Perdikaris, and Anuj Karpatne. Mitigating propagation failures in physics-informed neural networks using retain-resample-release (R3) sampling. In *Proceedings of the 40th International Conference on Machine Learning, ICML ’23*, pages 7264–7302, 2023.
- [23] Chenxi Wu, Min Zhu, Qinyang Tan, Yadhu Kartha, and Lu Lu. A comprehensive study of non-adaptive and residual-based adaptive sampling for physics-informed neural networks. *Computer Methods in Applied Mechanics and Engineering*, 403:115671, 2023.
- [24] Ping Zhu, Zhonglin Liu, Ziqing Xu, and Junxue Lv. An adaptive weight physics-informed neural network for vortex-induced vibration problems. *Buildings*, 15(9):1533, 2025.
- [25] Zixue Xiang, Wei Peng, Xu Liu, and Wen Yao. Self-adaptive loss balanced physics-informed neural networks. *Neurocomputing*, 496:11–34, 2022.
- [26] Zhao Chen, Vijay Badrinarayanan, Chen-Yu Lee, and Andrew Rabinovich. GradNorm: Gradient normalization for adaptive loss balancing in deep multitask networks. In *Proceedings of the 35th International Conference on Machine Learning, ICML ’18*, pages 794–803, 2018.
- [27] Jeremy Yu, Lu Lu, Xuhui Meng, and George Emmanouil Karniadakis. Gradient-enhanced physics-informed neural networks for forward and inverse PDE problems. *Computer Methods in Applied Mechanics and Engineering*, 393:114823, 2022.
- [28] Ze Tao, Hanxuan Wang, and Fujun Liu. LNN-PINN: A unified physics-only training framework with liquid residual blocks, 2025. arXiv preprint arXiv:2508.08935.
- [29] Shayan Dodge, Sami Barmada, and Alessandro Formisano. A stacked adaptive residual PINN (STAR-PINN) approach to 2D time-domain magnetic diffusion in nonlinear materials. *IEEE Access*, 13:141380–141394, 2025.
- [30] Mohammad Amin Nabian, Rini Jasmine Gladstone, and Hadi Meidani. Efficient training of physics-informed neural networks via importance sampling. *Computer-Aided Civil and Infrastructure Engineering*, 36(8):962–977, 2021.
- [31] Zhengqi Zhang, Jing Li, and Bin Liu. Annealed adaptive importance sampling method in PINNs for solving high dimensional partial differential equations. *Journal of Computational Physics*, 521:113561, 2025.
- [32] Yuling Jiao, Di Li, Xiliang Lu, Jerry Zhijian Yang, and Cheng Yuan. A Gaussian mixture distribution-based adaptive sampling method for physics-informed neural networks. *Engineering Applications of Artificial Intelligence*, 135:108770, 2024.
- [33] Khemraj Shukla, Ameya Dilip Jagtap, and George Emmanouil Karniadakis. Parallel physics-informed neural networks via domain decomposition. *Journal of Computational Physics*, 447:110683, 2021.

- [34] Ameya Dilip Jagtap and George Emmanouil Karniadakis. Extended physics-informed neural networks (XPINNs): A generalized space-time domain decomposition based deep learning framework for nonlinear partial differential equations. *Communications in Computational Physics*, 28(5):1605–1641, 2020.
- [35] Sifan Wang, Shyam Sankaran, and Paris Perdikaris. Respecting causality for training physics-informed neural networks. *Computer Methods in Applied Mechanics and Engineering*, 421:116813, 2024.
- [36] Dongkun Zhang, Lu Lu, Ling Guo, and George Emmanouil Karniadakis. Quantifying total uncertainty in physics-informed neural networks for solving forward and inverse stochastic problems. *Journal of Computational Physics*, 397:108850, 2019.
- [37] Yibo Yang and Paris Perdikaris. Adversarial uncertainty quantification in physics-informed neural networks. *Journal of Computational Physics*, 394:136–152, 2019.
- [38] Yoshua Bengio, Jérôme Louradour, Ronan Collobert, and Jason Weston. Curriculum learning. In *Proceedings of the 26th International Conference on Machine Learning*, ICML '09, pages 41–48, 2009.
- [39] Simone Monaco and Daniele Apiletti. Training physics-informed neural networks: One learning to rule them all? *Results in Engineering*, 18:101023, 2023.
- [40] Callum Duffy and Gergana Velikova. Dynamic curriculum regularization for enhanced training of physics-informed neural networks. In *NeurIPS 2024 Workshop on Machine Learning and the Physical Sciences (MLAPS)*, 2024.
- [41] Hasan Cetinkaya, Fahrettin Ay, Mehmet Tunçel, Hazem Nounou, Mohamed Numan Nounou, Hasan Kurban, and Erchin Serpedin. Curriculum-enhanced adaptive sampling for physics-informed neural networks: A robust framework for stiff PDEs. *Mathematics*, 13(24):3996, 2025.
- [42] Jianchuan Yang, Xuanqi Liu, Yu Diao, Xi Chen, and Haikuo Hu. Adaptive task decomposition physics-informed neural networks. *Computer Methods in Applied Mechanics and Engineering*, 418:116561, 2024.
- [43] Atılım Güneş Baydin, Barak Avrum Pearlmutter, Alexey Andreyevich Radul, and Jeffrey Mark Siskind. Automatic differentiation in machine learning: A survey. *Journal of Machine Learning Research*, 18(153):1–43, 2018.
- [44] Ehsan Haghghat, Maziar Raissi, Adrian Moure, Hector Gomez, and Ruben Juanes. A physics-informed deep learning framework for inversion and surrogate modeling in solid mechanics. *Computer Methods in Applied Mechanics and Engineering*, 379:113741, 2021.

## A. Theoretical Analysis and Proofs for CGMPINN

We analyze the optimization geometry induced by CGMPINN and a generalization bound for the weighted PDE objective when the weighting rule is fixed after a refresh step. Unless stated otherwise, notation follows Section 2; the GMM–curriculum construction is as in Eqs. (8)–(19) and the total loss is Eq. (23).

Convergence statements below concern *idealized* full-batch gradient descent on the time-varying total loss  $\mathcal{L}_{\text{total}}(\cdot; k)$ , which isolates GMM-based reweighting and objective drift. The hybrid Adam→L-BFGS procedure in experiments targets the same objective but is not analyzed iterate-wise here; what we establish are structural properties of the objective and of fixed-rule statistical risk (Remark A.23).

### A.1. Auxiliary Assumptions

We first state the assumptions used throughout the analysis.

**Assumption A.1** (Smoothness of the time-varying total loss). For every iteration  $k$ , the function  $\mathcal{L}_{\text{total}}(\cdot; k) : \mathbb{R}^p \rightarrow \mathbb{R}$  (where  $p$  is the parameter dimension introduced in Section 2) is continuously differentiable and  $L$ -smooth, namely

$$\|\nabla\theta\mathcal{L}_{\text{total}}(\theta_1; k) - \nabla\theta\mathcal{L}_{\text{total}}(\theta_2; k)\| \leq L\|\theta_1 - \theta_2\|, \quad \forall\theta_1, \theta_2 \in \mathbb{R}^p. \quad (\text{A.1})$$

Moreover,  $\mathcal{L}_{\text{total}}(\theta; k)$  admits a finite uniform lower bound: there exists  $\mathcal{L}_{\text{inf}} \in \mathbb{R}$  such that

$$\mathcal{L}_{\text{total}}(\theta; k) \geq \mathcal{L}_{\text{inf}}, \quad \forall\theta \in \mathbb{R}^p, k \geq 0. \quad (\text{A.2})$$

**Remark A.2** (Discussion of Assumption A.1). Both conditions are mild and standard in first-order optimization analysis of neural networks. The  $L$ -smoothness holds globally for networks with smooth activations (e.g., tanh, sigmoid, GELU, Swish) on any bounded parameter region, and almost everywhere for ReLU-type networks; in either case, the gradient remains Lipschitz on the compact iterate set encountered during training. The uniform lower bound is automatic for the composite MSE objective, since  $\mathcal{L}_{\text{total}}(\theta; k) \geq 0$  for every  $\theta$  and  $k$ , so we may take  $\mathcal{L}_{\text{inf}} = 0$ .

**Assumption A.3** (Bounded GMM variances). There exist constants  $0 < \underline{\sigma}^2 \leq \bar{\sigma}^2 < \infty$  such that, at every GMM refresh step and for every Gaussian component  $m$ ,

$$\underline{\sigma}^2 \leq \sigma_m^2 \leq \bar{\sigma}^2. \quad (\text{A.3})$$

**Remark A.4** (Discussion of Assumption A.3). The two-sided bound on  $\sigma_m^2$  is non-restrictive in practice. The upper bound  $\bar{\sigma}^2$  follows from the boundedness of PDE residuals on the compact training domain. The strict positive lower

bound  $\underline{\sigma}^2 > 0$  is routinely enforced in EM-based GMM solvers via covariance regularization (e.g., the `reg_covar` parameter of `scikit-learn`’s `GaussianMixture`), which adds a small floor to each component variance and rules out degenerate clusters.

**Assumption A.5** (Summable drift of the time-varying objective). Consider the full-batch gradient descent iteration

$$\theta_{k+1} = \theta_k - \eta\nabla\theta\mathcal{L}_{\text{total}}(\theta_k; k), \quad (\text{A.4})$$

with the step size  $\eta > 0$  as introduced in Theorem 2.3. Assume that there exists a nonnegative sequence  $\{\xi_k\}_{k \geq 0}$  such that

$$\sum_{k=0}^{\infty} \xi_k < \infty \quad (\text{A.5})$$

and

$$\mathcal{L}_{\text{total}}(\theta_{k+1}; k+1) - \mathcal{L}_{\text{total}}(\theta_{k+1}; k) \leq \xi_k, \quad \forall k. \quad (\text{A.6})$$

**Remark A.6** (Discussion of Assumption A.5). The objective drift in CGMPINN originates from three coupled sources: the curriculum parameter  $\tau(k)$ , the periodic GMM re-fitting that updates the sample weights  $\{w_i\}$ , and the ReLoBRaLo adaptive loss coefficients  $\{\lambda_c(k)\}$ . Summability of  $\xi_k$  is consistent with the design of CGMPINN. By Eq. (11), the curriculum parameter saturates at  $\tau(k) \equiv 1$  once  $k \geq k_{\text{max}} c_{\text{sat}}$ , after which the curriculum-induced drift vanishes identically. The GMM is refreshed only every  $k_{\text{upd}}$  iterations, and both its parameters  $\Theta_{\text{GMM}}$  and the resulting weights  $\{w_i\}$  stabilize as the residual distribution settles; an analogous stabilization occurs for the ReLoBRaLo weights through the EMA in Eq. (20). Together, these mechanisms ensure that  $\xi_k$  decays sufficiently fast to be summable, which validates the use of Assumption A.5 for the convergence analysis below.

### A.2. Convergence Analysis

#### A.2.1. EQUIVALENCE BETWEEN WEIGHTED AND STANDARD PDE LOSSES

**Theorem A.7** (Uniform equivalence between weighted and standard PDE losses). *Under Assumption A.3, define*

$$\underline{v} := \frac{\sigma^2 + \epsilon}{\bar{\sigma}^2 + \epsilon} \in (0, 1]. \quad (\text{A.7})$$

*Then, for every Gaussian component  $m$  and every curriculum parameter  $\tau \in [0, 1]$ , the component-level weight*

$$w_m^{\text{comp}}(\tau) = w_m^{\text{CL}}(\tau) \tilde{v}_m(\tau) \quad (\text{A.8})$$

*satisfies*

$$e^{-\beta} \underline{v} \leq w_m^{\text{comp}}(\tau) \leq 1. \quad (\text{A.9})$$

*Define the pre-normalized sample weight by*

$$w_i^{\text{raw}}(\tau) := \sum_{m=1}^K \gamma_{im} w_m^{\text{comp}}(\tau). \quad (\text{A.10})$$

Then

$$e^{-\beta \underline{v}} \leq w_i^{\text{raw}}(\tau) \leq 1. \quad (\text{A.11})$$

Let

$$\begin{aligned} c_- &:= \frac{N_\Omega e^{-\beta \underline{v}}}{N_\Omega + \epsilon}, \\ c_+ &:= \frac{N_\Omega}{N_\Omega e^{-\beta \underline{v}} + \epsilon}. \end{aligned} \quad (\text{A.12})$$

After the normalization in Eq. (18), the final sample weight  $w_i$  satisfies

$$c_- \leq w_i \leq c_+. \quad (\text{A.13})$$

Consequently, for every  $\theta$ ,

$$c_- \mathcal{L}_{\text{PDE}}(\theta) \leq \mathcal{L}_{\text{PDE}}^w(\theta) \leq c_+ \mathcal{L}_{\text{PDE}}(\theta). \quad (\text{A.14})$$

*Proof.* By Eq. (12),

$$w_m^{\text{easy}} = \exp(-\beta \tilde{d}_m), \quad w_m^{\text{hard}} = \exp(-\beta(1 - \tilde{d}_m)).$$

Since  $\tilde{d}_m \in [0, 1]$ , one has

$$e^{-\beta} \leq w_m^{\text{easy}} \leq 1, \quad e^{-\beta} \leq w_m^{\text{hard}} \leq 1. \quad (\text{A.15})$$

By Eq. (13),

$$w_m^{\text{CL}}(\tau) = (1 - \tau)w_m^{\text{easy}} + \tau w_m^{\text{hard}},$$

which is a convex combination of  $w_m^{\text{easy}}$  and  $w_m^{\text{hard}}$ . Hence,

$$e^{-\beta} \leq w_m^{\text{CL}}(\tau) \leq 1. \quad (\text{A.16})$$

Next, by Assumption A.3,

$$\frac{1}{\bar{\sigma}^2 + \epsilon} \leq (\sigma_m^2 + \epsilon)^{-1} \leq \frac{1}{\underline{\sigma}^2 + \epsilon}. \quad (\text{A.17})$$

Using Eq. (14), we have

$$v_m = \frac{(\sigma_m^2 + \epsilon)^{-1}}{\max_{1 \leq l \leq K} (\sigma_l^2 + \epsilon)^{-1}} \geq \frac{(\bar{\sigma}^2 + \epsilon)^{-1}}{(\underline{\sigma}^2 + \epsilon)^{-1}} = \frac{\underline{\sigma}^2 + \epsilon}{\bar{\sigma}^2 + \epsilon} = \underline{v}. \quad (\text{A.18})$$

Trivially,  $v_m \leq 1$ . Then by Eq. (15),

$$\underline{v} \leq \tilde{v}_m(\tau) \leq 1. \quad (\text{A.19})$$

Combining (A.16), (A.19), and Eq. (16), we obtain

$$e^{-\beta \underline{v}} \leq w_m^{\text{comp}}(\tau) = w_m^{\text{CL}}(\tau) \tilde{v}_m(\tau) \leq 1,$$

which proves (A.9).

Now consider the pre-normalized sample weight

$$w_i^{\text{raw}}(\tau) = \sum_{m=1}^K \gamma_{im} w_m^{\text{comp}}(\tau).$$

Since  $\gamma_{im} \geq 0$  and  $\sum_{m=1}^K \gamma_{im} = 1$  by Eq. (8),  $w_i^{\text{raw}}(\tau)$  is a convex combination of  $\{w_m^{\text{comp}}(\tau)\}_{m=1}^K$ . Therefore,

$$e^{-\beta \underline{v}} \leq w_i^{\text{raw}}(\tau) \leq 1,$$

which proves (A.11).

By Eq. (18), the final sample weight is

$$w_i = \frac{N_\Omega w_i^{\text{raw}}(\tau)}{\sum_{j=1}^{N_\Omega} w_j^{\text{raw}}(\tau) + \epsilon}. \quad (\text{A.20})$$

Using (A.11), we have

$$\sum_{j=1}^{N_\Omega} w_j^{\text{raw}}(\tau) \leq N_\Omega, \quad \sum_{j=1}^{N_\Omega} w_j^{\text{raw}}(\tau) \geq N_\Omega e^{-\beta \underline{v}}.$$

Substituting these bounds into (A.20) yields

$$w_i \geq \frac{N_\Omega e^{-\beta \underline{v}}}{N_\Omega + \epsilon} = c_-, \quad w_i \leq \frac{N_\Omega}{N_\Omega e^{-\beta \underline{v}} + \epsilon} = c_+,$$

which proves (A.13).

Finally, since  $r_{\text{PDE},i}^2 \geq 0$  for all  $i$ ,

$$\begin{aligned} \mathcal{L}_{\text{PDE}}^w(\theta) &= \frac{1}{N_\Omega} \sum_{i=1}^{N_\Omega} w_i r_{\text{PDE},i}^2 \\ &\geq \frac{1}{N_\Omega} \sum_{i=1}^{N_\Omega} c_- r_{\text{PDE},i}^2 \\ &= c_- \mathcal{L}_{\text{PDE}}(\theta), \end{aligned} \quad (\text{A.21})$$

and similarly,

$$\mathcal{L}_{\text{PDE}}^w(\theta) \leq c_+ \mathcal{L}_{\text{PDE}}(\theta). \quad (\text{A.22})$$

Combining (A.21) and (A.22) proves (A.14).  $\square$

**Corollary A.8** (Consistency with the standard PDE objective). *Under the assumptions of Theorem A.7, if a sequence  $\{\theta_n\}$  satisfies*

$$\mathcal{L}_{\text{PDE}}^w(\theta_n) \rightarrow 0, \quad (\text{A.23})$$

then necessarily

$$\mathcal{L}_{\text{PDE}}(\theta_n) \rightarrow 0. \quad (\text{A.24})$$

*Proof.* By (A.14),

$$0 \leq \mathcal{L}_{\text{PDE}}(\theta_n) \leq c_-^{-1} \mathcal{L}_{\text{PDE}}^w(\theta_n) \rightarrow 0. \quad (\text{A.25})$$

$\square$

## A.2.2. SUBLINEAR CONVERGENCE FOR THE TIME-VARYING TOTAL LOSS

**Theorem A.9** (Sublinear convergence of the time-varying total loss). *Suppose Assumptions A.1 and A.5 hold, and choose the step size  $\eta \in (0, 1/L]$ . Then the iterates generated by (A.4) satisfy*

$$\sum_{k=0}^{\infty} \|\nabla_{\theta} \mathcal{L}_{\text{total}}(\theta_k; k)\|^2 < \infty, \quad (\text{A.26})$$

where  $\Xi := \sum_{k=0}^{\infty} \xi_k$ . Moreover, for every integer  $K \geq 0$ ,

$$\begin{aligned} \min_{0 \leq t \leq K} \|\nabla_{\theta} \mathcal{L}_{\text{total}}(\theta_t; t)\|^2 &\leq \frac{2}{\eta(K+1)} \\ &\times \left( \mathcal{L}_{\text{total}}(\theta_0; 0) - \mathcal{L}_{\text{inf}} + \Xi \right). \end{aligned} \quad (\text{A.27})$$

Consequently,

$$\begin{aligned} \min_{0 \leq t \leq K} \|\nabla_{\theta} \mathcal{L}_{\text{total}}(\theta_t; t)\|^2 &= O(K^{-1}), \\ \|\nabla_{\theta} \mathcal{L}_{\text{total}}(\theta_k; k)\| &\rightarrow 0. \end{aligned} \quad (\text{A.28})$$

*Proof.* Since  $\mathcal{L}_{\text{total}}(\cdot; k)$  is  $L$ -smooth for each fixed  $k$ , the descent lemma yields

$$\begin{aligned} \mathcal{L}_{\text{total}}(\theta_{k+1}; k) &\leq \mathcal{L}_{\text{total}}(\theta_k; k) + \frac{L}{2} \|\theta_{k+1} - \theta_k\|^2 \\ &\quad + \left\langle \nabla_{\theta} \mathcal{L}_{\text{total}}(\theta_k; k), \theta_{k+1} - \theta_k \right\rangle \end{aligned} \quad (\text{A.29})$$

Substituting the update rule (A.4), we obtain

$$\begin{aligned} \mathcal{L}_{\text{total}}(\theta_{k+1}; k) &\leq \mathcal{L}_{\text{total}}(\theta_k; k) - \eta \|\nabla_{\theta} \mathcal{L}_{\text{total}}(\theta_k; k)\|^2 \\ &\quad + \frac{L\eta^2}{2} \|\nabla_{\theta} \mathcal{L}_{\text{total}}(\theta_k; k)\|^2. \end{aligned} \quad (\text{A.30})$$

Since  $\eta \leq 1/L$ , one has  $1 - \frac{L\eta}{2} \geq \frac{1}{2}$ , and therefore

$$\mathcal{L}_{\text{total}}(\theta_{k+1}; k) \leq \mathcal{L}_{\text{total}}(\theta_k; k) - \frac{\eta}{2} \|\nabla_{\theta} \mathcal{L}_{\text{total}}(\theta_k; k)\|^2. \quad (\text{A.31})$$

By Assumption A.5,

$$\mathcal{L}_{\text{total}}(\theta_{k+1}; k+1) - \mathcal{L}_{\text{total}}(\theta_{k+1}; k) \leq \xi_k. \quad (\text{A.32})$$

Combining (A.31) and (A.32), we obtain

$$\mathcal{L}_{\text{total}}(\theta_{k+1}; k+1) \leq \mathcal{L}_{\text{total}}(\theta_k; k) - \frac{\eta}{2} \|\nabla_{\theta} \mathcal{L}_{\text{total}}(\theta_k; k)\|^2 + \xi_k \cdot \|\nabla_{\theta} \mathcal{L}_{\text{total}}(\bar{\theta}; k_j) - \nabla_{\theta} \mathcal{L}_{\text{total}}(\theta_{k_j}; k_j)\| \leq L \|\bar{\theta} - \theta_{k_j}\| \rightarrow 0. \quad (\text{A.33})$$

Summing (A.33) from  $k = 0$  to  $K$  yields

$$\begin{aligned} \mathcal{L}_{\text{total}}(\theta_{K+1}; K+1) &\leq \mathcal{L}_{\text{total}}(\theta_0; 0) + \sum_{k=0}^K \xi_k \\ &\quad - \frac{\eta}{2} \sum_{k=0}^K \|\nabla_{\theta} \mathcal{L}_{\text{total}}(\theta_k; k)\|^2. \end{aligned} \quad (\text{A.34})$$

Using the lower bound  $\mathcal{L}_{\text{total}}(\theta_{K+1}; K+1) \geq \mathcal{L}_{\text{inf}}$ , we obtain

$$\begin{aligned} \frac{\eta}{2} \sum_{k=0}^K \|\nabla_{\theta} \mathcal{L}_{\text{total}}(\theta_k; k)\|^2 &\leq \mathcal{L}_{\text{total}}(\theta_0; 0) - \mathcal{L}_{\text{inf}} + \sum_{k=0}^K \xi_k \\ &\leq \mathcal{L}_{\text{total}}(\theta_0; 0) - \mathcal{L}_{\text{inf}} + \Xi. \end{aligned} \quad (\text{A.35})$$

Letting  $K \rightarrow \infty$  proves (A.26).

Moreover,

$$(K+1) \min_{0 \leq t \leq K} \|\nabla_{\theta} \mathcal{L}_{\text{total}}(\theta_t; t)\|^2 \leq \sum_{k=0}^K \|\nabla_{\theta} \mathcal{L}_{\text{total}}(\theta_k; k)\|^2. \quad (\text{A.36})$$

Combining (A.35) and (A.36) gives (A.27).

Finally, since the nonnegative series in (A.26) converges, its general term must converge to zero, which proves (A.28).  $\square$

**Corollary A.10** (Stationarity of accumulation points). *Assume, in addition to Theorem A.9, that the sequence  $\{\theta_k\}$  is bounded and that there exists a continuously differentiable limit objective  $\mathcal{L}_{\infty}(\theta)$  such that*

$$\sup_{\theta \in \mathcal{K}} \|\nabla_{\theta} \mathcal{L}_{\text{total}}(\theta; k) - \nabla_{\theta} \mathcal{L}_{\infty}(\theta)\| \rightarrow 0, \quad (\text{A.37})$$

for every compact  $\mathcal{K} \subset \mathbb{R}^p$ .

Then every accumulation point of  $\{\theta_k\}$  is a stationary point of  $\mathcal{L}_{\infty}(\theta)$ .

*Proof.* Let  $\bar{\theta}$  be an accumulation point of  $\{\theta_k\}$ . Then there exists a subsequence  $\{\theta_{k_j}\}$  such that  $\theta_{k_j} \rightarrow \bar{\theta}$ . Since  $\{\theta_k\}$  is bounded, all  $\theta_{k_j}$  and  $\bar{\theta}$  belong to a common compact set  $\mathcal{K}$ . We write

$$\begin{aligned} \|\nabla_{\theta} \mathcal{L}_{\infty}(\bar{\theta})\| &\leq \|\nabla_{\theta} \mathcal{L}_{\infty}(\bar{\theta}) - \nabla_{\theta} \mathcal{L}_{\text{total}}(\bar{\theta}; k_j)\| \\ &\quad + \|\nabla_{\theta} \mathcal{L}_{\text{total}}(\bar{\theta}; k_j) - \nabla_{\theta} \mathcal{L}_{\text{total}}(\theta_{k_j}; k_j)\| \\ &\quad + \|\nabla_{\theta} \mathcal{L}_{\text{total}}(\theta_{k_j}; k_j)\|. \end{aligned} \quad (\text{A.38})$$

The first term tends to zero by (A.37). The second term tends to zero by Assumption A.1:

$$\|\nabla_{\theta} \mathcal{L}_{\text{total}}(\bar{\theta}; k_j) - \nabla_{\theta} \mathcal{L}_{\text{total}}(\theta_{k_j}; k_j)\| \leq L \|\bar{\theta} - \theta_{k_j}\| \rightarrow 0. \quad (\text{A.39})$$

The third term tends to zero by (A.28). Hence,

$$\nabla_{\theta} \mathcal{L}_{\infty}(\bar{\theta}) = 0. \quad (\text{A.40})$$

□

### A.2.3. PL-BASED CONVERGENCE WITH DRIFT CONTROL

**Assumption A.11** (Uniform Polyak–Łojasiewicz condition with a common reference level). There exist constants  $\mu > 0$  and  $\mathcal{L}^* \in \mathbb{R}$  such that, for every  $k$  and every  $\theta$ ,

$$\mathcal{L}_{\text{total}}(\theta; k) \geq \mathcal{L}^*, \quad (\text{A.41})$$

and

$$\frac{1}{2} \|\nabla_{\theta} \mathcal{L}_{\text{total}}(\theta; k)\|^2 \geq \mu(\mathcal{L}_{\text{total}}(\theta; k) - \mathcal{L}^*). \quad (\text{A.42})$$

**Assumption A.12** (Uniformly bounded drift amplitude). In addition to Assumption A.5, assume that there exists  $\bar{\xi} \geq 0$  such that

$$0 \leq \xi_k \leq \bar{\xi}, \quad \forall k. \quad (\text{A.43})$$

**Theorem A.13** (PL-based convergence to a drift-controlled neighborhood). Suppose Assumptions A.1, A.11, and A.12 hold, and choose  $\eta \in (0, 1/L]$ . Define the objective gap

$$E_k := \mathcal{L}_{\text{total}}(\theta_k; k) - \mathcal{L}^*. \quad (\text{A.44})$$

Then

$$E_{k+1} \leq (1 - \eta\mu)E_k + \xi_k. \quad (\text{A.45})$$

Consequently, for every  $k \geq 0$ ,

$$E_k \leq (1 - \eta\mu)^k E_0 + \sum_{t=0}^{k-1} (1 - \eta\mu)^{k-1-t} \xi_t. \quad (\text{A.46})$$

In particular, since  $\xi_t \leq \bar{\xi}$ ,

$$\begin{aligned} E_k &\leq (1 - \eta\mu)^k E_0 + \frac{\bar{\xi}}{\eta\mu} \left(1 - (1 - \eta\mu)^k\right) \\ &\leq (1 - \eta\mu)^k E_0 + \frac{\bar{\xi}}{\eta\mu}. \end{aligned} \quad (\text{A.47})$$

Hence,

$$\limsup_{k \rightarrow \infty} E_k \leq \frac{\bar{\xi}}{\eta\mu}. \quad (\text{A.48})$$

That is, the homogeneous term decays linearly, and the total loss is controlled by a drift-dominated neighborhood whose radius is proportional to  $\bar{\xi}/(\eta\mu)$ .

*Proof.* From (A.33), we already have

$$\begin{aligned} \mathcal{L}_{\text{total}}(\theta_{k+1}; k+1) &\leq \mathcal{L}_{\text{total}}(\theta_k; k) + \xi_k \\ &\quad - \frac{\eta}{2} \|\nabla_{\theta} \mathcal{L}_{\text{total}}(\theta_k; k)\|^2. \end{aligned} \quad (\text{A.49})$$

By Assumption A.11,

$$\frac{1}{2} \|\nabla_{\theta} \mathcal{L}_{\text{total}}(\theta_k; k)\|^2 \geq \mu(\mathcal{L}_{\text{total}}(\theta_k; k) - \mathcal{L}^*) = \mu E_k. \quad (\text{A.50})$$

Substituting (A.50) into (A.49) yields

$$\mathcal{L}_{\text{total}}(\theta_{k+1}; k+1) \leq \mathcal{L}_{\text{total}}(\theta_k; k) - \eta\mu E_k + \xi_k. \quad (\text{A.51})$$

Subtracting  $\mathcal{L}^*$  from both sides gives (A.45).

Let  $q := 1 - \eta\mu$ . By induction on  $k$ , (A.45) implies (A.46). Using  $\xi_t \leq \bar{\xi}$ , we further obtain

$$\sum_{t=0}^{k-1} q^{k-1-t} \xi_t \leq \bar{\xi} \sum_{j=0}^{k-1} q^j = \bar{\xi} \frac{1 - q^k}{1 - q} = \bar{\xi} \frac{1 - (1 - \eta\mu)^k}{\eta\mu}, \quad (\text{A.52})$$

which yields (A.47). Taking the limit superior proves (A.48). □

**Corollary A.14** (Exact convergence under summable drift). Under the assumptions of Theorem A.13, if in addition Assumption A.5 holds, namely  $\sum_{k=0}^{\infty} \xi_k < \infty$ , then

$$E_k \rightarrow 0, \quad \text{i.e.,} \quad \mathcal{L}_{\text{total}}(\theta_k; k) \rightarrow \mathcal{L}^*. \quad (\text{A.53})$$

*Proof.* From (A.46), it suffices to show that

$$\sum_{t=0}^{k-1} (1 - \eta\mu)^{k-1-t} \xi_t \rightarrow 0.$$

Let  $q := 1 - \eta\mu \in [0, 1)$ . Since  $\sum_{t=0}^{\infty} \xi_t < \infty$ , for any  $\varepsilon > 0$  (local proof variable, distinct from the global numerical constant  $\varepsilon$ ) there exists a threshold index  $T_0$  (not to be confused with the final time  $T$  in Section 2) such that

$$\sum_{t=T_0}^{\infty} \xi_t < \frac{\varepsilon}{2}.$$

For every  $k > T_0$ ,

$$\begin{aligned} \sum_{t=0}^{k-1} q^{k-1-t} \xi_t &= \sum_{t=0}^{T_0-1} q^{k-1-t} \xi_t + \sum_{t=T_0}^{k-1} q^{k-1-t} \xi_t \\ &\leq q^{k-T_0} \sum_{t=0}^{T_0-1} \xi_t + \sum_{t=T_0}^{k-1} \xi_t. \end{aligned} \quad (\text{A.54})$$

The second term is smaller than  $\varepsilon/2$  by construction. The first term tends to zero as  $k \rightarrow \infty$  because  $q \in [0, 1)$ . Hence, for all sufficiently large  $k$ ,

$$\sum_{t=0}^{k-1} q^{k-1-t} \xi_t < \varepsilon.$$

Therefore,

$$\sum_{t=0}^{k-1} q^{k-1-t} \xi_t \rightarrow 0.$$

Together with (A.46) and  $q^k E_0 \rightarrow 0$ , this proves (A.53).  $\square$

**Corollary A.15** (Exact linear convergence in the zero-drift case). *Under the assumptions of Theorem A.13, if  $\xi_k \equiv 0$ , then*

$$E_k \leq (1 - \eta\mu)^k E_0, \quad \forall k \geq 0. \quad (\text{A.55})$$

Hence,

$$\mathcal{L}_{\text{total}}(\theta_k; k) \rightarrow \mathcal{L}^* \quad \text{at a linear rate.} \quad (\text{A.56})$$

*Proof.* Setting  $\xi_k \equiv 0$  in (A.46) immediately gives (A.55), from which (A.56) follows.  $\square$

### A.3. Generalization Analysis

To distinguish population risks from empirical losses, we define

$$\mathcal{E}_{\text{PDE}}(\theta) := \mathbb{E}_{(\mathbf{x}, t) \sim \rho} [r_{\text{PDE}}^2(\mathbf{x}, t; \theta)], \quad (\text{A.57})$$

and

$$\mathcal{E}_{\text{PDE}}^w(\theta) := \mathbb{E}_{(\mathbf{x}, t) \sim \rho} [w(\mathbf{x}, t) r_{\text{PDE}}^2(\mathbf{x}, t; \theta)], \quad (\text{A.58})$$

where  $w(\mathbf{x}, t)$  denotes the pointwise weight induced by the same GMM-curriculum mechanism.

**Assumption A.16** (Bounded residual class). There exists a constant  $M > 0$  such that, for all  $\theta$  and all  $(\mathbf{x}, t) \in \Omega \times [0, T]$ ,

$$|r_{\text{PDE}}(\mathbf{x}, t; \theta)| \leq M. \quad (\text{A.59})$$

Equivalently,

$$0 \leq r_{\text{PDE}}^2(\mathbf{x}, t; \theta) \leq B := M^2. \quad (\text{A.60})$$

**Assumption A.17** (Bounded weight function). There exists a constant  $W \geq 1$  such that

$$0 \leq w(\mathbf{x}, t) \leq W, \quad \forall (\mathbf{x}, t) \in \Omega \times [0, T]. \quad (\text{A.61})$$

**Split-sample proof device.** We decouple weight construction from the empirical process by fitting the GMM on a reference sample and forming  $w(\mathbf{x}, t)$  from it; a separate sample defines the weighted empirical loss

$$\mathcal{L}_{\text{PDE}}^w(\theta) = \frac{1}{N_\Omega} \sum_{i=1}^{N_\Omega} w(\mathbf{x}_i, t_i) r_{\text{PDE}, i}^2. \quad (\text{A.62})$$

Conditioned on the reference draw,  $w$  is deterministic (whereas the implementation may reuse the same collocation points). The bound below is for a fixed refresh/frozen rule and does not address fully coupled adaptive reweighting across all iterations.

Let  $\Theta \subseteq \mathbb{R}^p$  denote the parameter space over which the network is optimized, and define the squared-residual function class

$$\mathcal{F} := \{(\mathbf{x}, t) \mapsto r_{\text{PDE}}^2(\mathbf{x}, t; \theta) : \theta \in \Theta\}. \quad (\text{A.63})$$

**Theorem A.18** (Generalization bound for the weighted empirical PDE loss under a frozen weighting rule). *Under Assumptions A.16 and A.17, conditioned on the reference sample used to construct  $w(\mathbf{x}, t)$ , with probability at least  $1 - \delta$  over the independent training sample  $\{(\mathbf{x}_i, t_i)\}_{i=1}^{N_\Omega}$ , the following holds simultaneously for all  $\theta \in \Theta$ :*

$$\begin{aligned} \mathcal{E}_{\text{PDE}}^w(\theta) &\leq \mathcal{L}_{\text{PDE}}^w(\theta) + 2W \mathfrak{R}_{N_\Omega}(\mathcal{F}) \\ &\quad + 3BW \sqrt{\frac{\log(2/\delta)}{2N_\Omega}}. \end{aligned} \quad (\text{A.64})$$

where  $\mathfrak{R}_{N_\Omega}(\mathcal{F})$  denotes the Rademacher complexity of  $\mathcal{F}$ .

*Proof.* Define the weighted function class

$$w\mathcal{F} := \{(\mathbf{x}, t) \mapsto w(\mathbf{x}, t) r_{\text{PDE}}^2(\mathbf{x}, t; \theta) : \theta \in \Theta\}. \quad (\text{A.65})$$

Since  $0 \leq r_{\text{PDE}}^2(\mathbf{x}, t; \theta) \leq B$  and  $0 \leq w(\mathbf{x}, t) \leq W$ , every function in  $w\mathcal{F}$  is bounded in  $[0, BW]$ .

By the standard Rademacher-complexity-based uniform convergence bound, with probability at least  $1 - \delta$ ,

$$\begin{aligned} \sup_{\theta \in \Theta} \left( \mathcal{E}_{\text{PDE}}^w(\theta) - \mathcal{L}_{\text{PDE}}^w(\theta) \right) &\leq 2 \mathfrak{R}_{N_\Omega}(w\mathcal{F}) \\ &\quad + 3BW \sqrt{\frac{\log(2/\delta)}{2N_\Omega}}. \end{aligned} \quad (\text{A.66})$$

It therefore suffices to estimate  $\mathfrak{R}_{N_\Omega}(w\mathcal{F})$ . For a fixed training sample,

$$\widehat{\mathfrak{R}}(w\mathcal{F}) = \mathbb{E}_\sigma \left[ \sup_{\theta \in \Theta} \frac{1}{N_\Omega} \sum_{i=1}^{N_\Omega} \sigma_i w(\mathbf{x}_i, t_i) r_{\text{PDE}, i}^2 \right], \quad (\text{A.67})$$

where  $\{\sigma_i\}_{i=1}^{N_\Omega}$  are i.i.d. Rademacher random variables (not to be confused with the GMM component variances  $\sigma_m^2$  in Section 2). For each  $i$ , the map  $\phi_i(u) = w(\mathbf{x}_i, t_i)u$  satisfies  $\phi_i(0) = 0$  and is  $W$ -Lipschitz. Hence, by the contraction inequality,

$$\widehat{\mathfrak{R}}(w\mathcal{F}) \leq W \widehat{\mathfrak{R}}(\mathcal{F}). \quad (\text{A.68})$$

Taking expectation over the training sample yields

$$\mathfrak{R}_{N_\Omega}(w\mathcal{F}) \leq W \mathfrak{R}_{N_\Omega}(\mathcal{F}). \quad (\text{A.69})$$

Substituting (A.69) into (A.66) proves (A.64).  $\square$

**Corollary A.19** (Generalization bound for the original PDE risk under a frozen weight rule). *Under the assumptions of Theorem A.18, with probability at least  $1 - \delta$ , uniformly for all  $\theta \in \Theta$ ,*

$$\begin{aligned} \mathcal{E}_{\text{PDE}}(\theta) &\leq \mathcal{L}_{\text{PDE}}^w(\theta) + 2W \mathfrak{R}_{N_\Omega}(\mathcal{F}) \\ &\quad + 3BW \sqrt{\frac{\log(2/\delta)}{2N_\Omega}} + B \|w - 1\|_{L^1(\rho)}. \end{aligned} \quad (\text{A.70})$$

*Proof.* By definition,

$$\mathcal{E}_{\text{PDE}}(\theta) - \mathcal{E}_{\text{PDE}}^w(\theta) = \mathbb{E}_{(\mathbf{x}, t) \sim \rho} \left[ (1 - w(\mathbf{x}, t)) r_{\text{PDE}}^2(\mathbf{x}, t; \theta) \right]. \quad (\text{A.71})$$

Taking absolute values and using (A.60), we obtain

$$\begin{aligned} |\mathcal{E}_{\text{PDE}}(\theta) - \mathcal{E}_{\text{PDE}}^w(\theta)| &\leq B \mathbb{E}_{(\mathbf{x}, t) \sim \rho} |1 - w(\mathbf{x}, t)| \\ &= B \|w - 1\|_{L^1(\rho)}. \end{aligned} \quad (\text{A.72})$$

Therefore,

$$\mathcal{E}_{\text{PDE}}(\theta) \leq \mathcal{E}_{\text{PDE}}^w(\theta) + B \|w - 1\|_{L^1(\rho)}. \quad (\text{A.73})$$

Applying Theorem A.18 to  $\mathcal{E}_{\text{PDE}}^w(\theta)$  yields (A.70).  $\square$

**Corollary A.20** (Pseudo-dimension form). *Assume, in addition, that the pseudo-dimension of  $\mathcal{F}$  is  $d_{\mathcal{F}}$  (not to be confused with the spatial dimension  $d$  of  $\Omega$  in Section 2). Then there exists a universal constant  $C_{\text{R}} > 0$  (distinct from the convergence constant  $C$  in Theorem 2.3) such that, with probability at least  $1 - \delta$ ,*

$$\begin{aligned} \mathcal{E}_{\text{PDE}}(\theta) &\leq \mathcal{L}_{\text{PDE}}^w(\theta) + C_{\text{R}} B W \sqrt{\frac{d_{\mathcal{F}} \log(e N_{\Omega} / d_{\mathcal{F}}) + \log(1/\delta)}{N_{\Omega}}} \\ &\quad + B \|w - 1\|_{L^1(\rho)}, \quad \forall \theta \in \Theta. \end{aligned} \quad (\text{A.74})$$

*Proof.* For uniformly bounded function classes with pseudo-dimension  $d_{\mathcal{F}}$ , the standard Rademacher complexity estimate yields

$$\mathfrak{R}_{N_{\Omega}}(\mathcal{F}) \leq C_{\text{R}} B \sqrt{\frac{d_{\mathcal{F}} \log(e N_{\Omega} / d_{\mathcal{F}})}{N_{\Omega}}}. \quad (\text{A.75})$$

Substituting (A.75) into (A.70) proves the claim.  $\square$

*Remark A.21* (Interpretation of the frozen-rule generalization result). Theorem A.18 characterizes the statistical behavior of the induced weighted empirical PDE objective at a fixed refresh step after the weighting rule has been frozen. It therefore provides a clean generalization guarantee for the induced weighted objective, but it should not be interpreted as a complete generalization theory for the fully coupled adaptive reweighting process across all training iterations.

*Remark A.22* (Interpretation of the bias term). The additional term  $B \|w - 1\|_{L^1(\rho)}$  in (A.70) quantifies the bias incurred by optimizing the weighted PDE risk instead of the original unweighted one. Under the current CGMPINN design, this term does not automatically vanish as  $\tau(k) \rightarrow 1$ , because the terminal hard-curriculum weights remain difficulty-dependent. If asymptotically unbiased weighting is desired, an additional design constraint must be imposed, for example by explicitly forcing the terminal component weights to approach 1.

*Remark A.23* (What the appendix establishes and what it does not). The results support three claims: (i) uniform equivalence of the curriculum-weighted and standard empirical PDE losses; (ii) stationarity-type guarantees for idealized full-batch descent on the time-varying total loss under summable objective drift; and (iii) a standard uniform convergence bound for the weighted empirical PDE loss at a fixed refresh step (frozen weights), plus an explicit bias term toward the unweighted population risk. They do not furnish iterate-level convergence for Adam→L-BFGS nor prove that CGMPINN strictly improves generalization over standard PINNs; a rigorous analysis of the hybrid optimizer under adaptive reweighting is left to future work.

## B. Ablation Study

To disentangle the contributions of the two core components in CGMPINN—the GMM-based difficulty quantification and the curriculum learning schedule—we conduct an ablation study across all benchmark PDEs. Three variants are compared:

- **GMPINN** (GMM-based weighting only): A GMM is fitted to the PDE residuals and component-level difficulty scores are computed, but no curriculum schedule is applied. Instead, the component weights are set to  $\exp(\beta \tilde{d}_m)$ , which statically up-weights harder components throughout training. The precision-based variance factor, when enabled, is applied without  $\tau$ -modulation.
- **CLPINN** (curriculum learning only): The  $\tau$ -controlled easy-to-hard curriculum schedule is applied, but difficulty is measured per-sample from the raw squared residual magnitude rather than from GMM component-level statistics. No GMM fitting or precision modulation is used.
- **CGMPINN** (full framework): The complete method combining GMM-based component-level difficulty quantification,  $\tau$ -controlled curriculum scheduling, and precision-based variance modulation, as described in Section 2.

All problem configurations, network architectures, training hyperparameters, and evaluation metrics are identical to those in Section 3. The Adam→L-BFGS two-stage optimization strategy is used for all three variants.

Table 13 reports the ablation results. CGMPINN consistently achieves the lowest  $e_2$ , relative  $e_2$ , and  $e_{\infty}$  across all benchmarks, confirming that neither component alone matches the performance of their combination.

**1D Poisson.** GMPINN fails catastrophically ( $e_2 = 2.17$ ), demonstrating that statically up-weighting high-residual re-

Table 13. Ablation study comparing GMMPINN, CLPINN, and CGMPINN on all benchmark PDEs. All experimental settings are identical to those in Section 3. Bold indicates the best result in each group.

Problem	Method	$e_{\text{Loss}}$	$e_2$	Relative $e_2$	$e_\infty$	CPU (s)
1D Poisson	GMMPINN	3.68e+3	2.17e+0	2.01e+0	3.53e+0	821.4
	CLPINN	2.34e-3	3.29e-3	3.04e-3	4.22e-3	818.9
	CGMPINN	<b>7.40e-4</b>	<b>1.96e-4</b>	<b>1.81e-4</b>	<b>3.73e-4</b>	895.9
2D Poisson	GMMPINN	2.97e-4	5.66e-4	7.10e-4	3.39e-3	1442.0
	CLPINN	7.59e-5	5.39e-4	6.76e-4	4.80e-3	1575.8
	CGMPINN	<b>6.65e-5</b>	<b>4.65e-4</b>	<b>5.83e-4</b>	<b>2.95e-3</b>	1453.2
Heat	GMMPINN	2.76e-2	1.79e-3	1.57e-3	2.29e-2	1010.7
	CLPINN	9.90e-5	1.78e-3	1.56e-3	2.51e-2	1216.6
	CGMPINN	<b>1.28e-5</b>	<b>4.04e-4</b>	<b>3.54e-4</b>	<b>2.86e-3</b>	1429.96
Damped Wave	GMMPINN	2.11e-6	4.36e-4	9.15e-4	3.00e-3	617.0
	CLPINN	2.92e-6	5.10e-4	1.07e-3	3.92e-3	581.0
	CGMPINN	<b>1.56e-6</b>	<b>3.37e-4</b>	<b>7.07e-4</b>	<b>2.20e-3</b>	678.0
Advection-Diffusion	GMMPINN	3.18e-6	6.87e-4	1.02e-3	1.43e-3	517.9
	CLPINN	<b>1.41e-6</b>	3.37e-4	5.00e-4	9.71e-4	517.4
	CGMPINN	1.66e-6	<b>2.57e-4</b>	<b>3.82e-4</b>	<b>7.14e-4</b>	532.4
Fisher-KPP	GMMPINN	1.54e-6	3.06e-3	3.97e-3	1.18e-2	1632.9
	CLPINN	1.00e-6	1.25e-3	1.63e-3	4.51e-3	1602.3
	CGMPINN	<b>3.12e-7</b>	<b>7.64e-4</b>	<b>9.94e-4</b>	<b>4.00e-3</b>	1722.9

gions without a curriculum schedule overwhelms the optimizer early in training and leads to divergence. CLPINN achieves reasonable accuracy ( $e_2 = 3.29 \times 10^{-3}$ ), but CGMPINN further reduces the error by over an order of magnitude ( $e_2 = 1.96 \times 10^{-4}$ ), indicating that the GMM-based structural information significantly enhances the per-sample curriculum when properly integrated.

**2D Poisson.** All three variants achieve comparable accuracy, with CGMPINN providing modest improvements in both  $e_2$  and  $e_\infty$ . The relatively uniform difficulty landscape of this problem reduces the benefit of structured difficulty quantification, though the GMM-curriculum combination still yields the best overall performance.

**Heat equation.** GMMPINN and CLPINN yield similar  $e_2$  values ( $\approx 1.8 \times 10^{-3}$ ), but CGMPINN reduces the error by approximately  $4\times$  to  $4.04 \times 10^{-4}$ . This suggests that the multi-scale temporal dynamics in the heat equation benefit substantially from the combination of component-level difficulty quantification and progressive curriculum scheduling.

**Damped wave equation.** CGMPINN achieves the lowest errors among the three variants, reducing  $e_2$  by 23% relative to GMMPINN and 34% relative to CLPINN. Notably, CLPINN performs slightly worse than GMMPINN on this problem, suggesting that for oscillatory solutions the GMM-based clustering captures difficulty structure more

effectively than per-sample residual magnitude alone.

**Advection-diffusion equation.** CLPINN already provides a substantial improvement over GMMPINN ( $e_2$  reduced by 51%), reflecting the importance of progressive curriculum scheduling for advection-dominated problems where sharp fronts emerge. CGMPINN further reduces the error by 24% relative to CLPINN, confirming the added value of the GMM-based difficulty quantification.

**Fisher-KPP equation.** Both components contribute meaningfully: CLPINN reduces  $e_2$  by 59% relative to GMMPINN, and CGMPINN achieves an additional 39% reduction over CLPINN. The nonlinear traveling-wave dynamics of this problem benefit from both the structured difficulty identification and the progressive training schedule.

In summary, the ablation study confirms that the two components of CGMPINN—GMM-based difficulty quantification and curriculum scheduling—are complementary. The GMM module provides structured, component-level difficulty information that the per-sample curriculum alone cannot capture, while the curriculum schedule prevents the premature focus on hard regions that causes GMMPINN to fail on challenging problems. Their combination consistently yields the best performance, with the most pronounced advantages on problems featuring strong nonlinearity, multi-scale dynamics, or sharp gradients.